ELSEVIER

Contents lists available at ScienceDirect

International Journal of Fatigue

journal homepage: www.elsevier.com/locate/ijfatigue





Thermo-mechanical fatigue induced unexpected strain hardening of Cu clip wiring on transfer-mold type EV power modules

Dongjin Kim^{a,*}, Seungjun Noh^b, Semin Park^b, Min-Su Kim^{a,*}

- ^a Advanced Joining and Additive Manufacturing R&D Department, Korea Institute of Industrial Technology (KITECH), 156, Gaetbeol-ro, Yeonsu-gu, Incheon 21999, Republic of Korea
- b Power Semiconductor Module Development Cell, Hyundai Mobis Co., Ltd., 17-2, Mabuk-ro 240beon-gil, Giheung-gu, Yongin-si, Gyeonggi-do 16891, Republic of Korea

ARTICLE INFO

Keywords:
Cu clip wire
Strain hardening
Thermomechanical fatigue
FEM
EBSD

ABSTRACT

Power modules subjected to cyclic power operation experience thermomechanical fatigue. Herein, the epoxy molding compounds and creep behaviors of solder joints promoted the strain hardening of the Cu clip wiring and caused failure to the power module during the power operations. In the Cu clips, the grain size was refined by 90% from the failure stage compared to the initial state, and an increase in hardness was observed. The results indicate that constraints of EMC and the creep behaviors of solder joints are other critical factors for the role of bare Cu clip strain hardening of EV power modules.

1. Introduction

One of our choices for a sustainable planet is the transition to green cars. Some of the key performances for the next-generation eco-friendly vehicle systems are the miniaturization and high efficiency of a power conversion system, a power inverter, and a converter. The power module of an inverter system is the key component in the power conversion system due to the role it plays in converting the direct current (DC) to alternating current (AC) [1]. The power inverter plays a decisive role in controlling the motor by converting the DC voltage of the battery into AC. At the heart of the power inverter are power semiconductor devices arranged in multi-chip power modules that control the motor torque and speed by means of pulse width modulation [2]. Current issues of the power module in pursuit of miniaturization have to withstand the higher operating temperature more than typical Si power modules due to driving energy loss from higher voltage operations by emerging the wide band-gap power devices [3,4]. In recent years, to cope with thermal dissipation and high energy density of power modules effectively, thermal design technologies such as double-sided cooling (DSC), ribbon bonding and clip bonding [5] are emerging to implement the thermal management technologies [6-8]. Amongst parts of the power module, a direct bonded copper (DBC) is a type of substrate in which Cu is directly bonded to the top and bottom of a ceramic substrate (Al₂O₃, AlN, Si₃N₄, etc.), and is a component responsible for heat dissipation and electrically insulation of the power module [9]. The Hybrid PACK of Infineon (2016) is a typical DSC power module composed of both sides of DBC substrates.

Nevertheless, it has been reported that Cu of the DBC cracks ceramics due to the significant strain hardening and hardness increasing in thermal shock environments compared to the bare Cu [10,11]. It is well known that the thermal fatigue of the DBC substrate limits the lifetime of the power module [12]. In addition, it is well known that strain hardening and thermomechanical fatigue were found to be strongly dependent on the substrate layout [10,13]. In this context, bare Cu clip wire interconnection without DBC substrates (i.e., DBC-less electronics) based on excellent electrical properties can be a good alternative to reduce thermal issues. Moreover, the clip-type interconnection has an additional option of assembling the heat sink on top of the clip or using a thick clip for dual-side cooling [14]. However, to apply to vehicles with a long warranty period, even if bare Cu clip wire interconnection is applied to actual products of the power module, we need a deep understanding of whether there are issues with malfunctions, i.e., failures with strain hardening. Because, even below the recrystallization temperature (less than 250 °C), it has been reported that the mechanical properties were lowered due to fundamental changes in the microstructure of high-purity Cu films due to thermos-mechanical fatigue [15]. Moreover, it has been reported that the heel crack or lift-off of wire bonding accounts for most of the failure modes of the conventional power module [16-18]. For this reason, since the Cu clip also acts as a wire, it is very important to scientifically consider the degradation of the Cu clip itself or the change in its behavior. In particular, this is currently a major challenge facing automakers dealing with power modules. The

E-mail addresses: dongjinkim@kitech.re.kr (D. Kim), mskim927@kitech.re.kr (M.-S. Kim).

^{*} Corresponding authors.

Nomenclatures		ε	Strain [-]	
		δl	Elongated length [m]	
Symbols		l_0	Length of initial condition [m]	
T _{jmax}	Maximum junction temperature [°C]	ε_e	Term of elastic strain [-]	
T_c	Case temperature [°C]	$arepsilon_p$	Term of plastic strain [-]	
ΔT_j	Temperature swing [°C]	σ_{eq}	Equivalent stress [Pa]	
P_{D}	Power dissipation of power device [W]			
R _{th}	Thermal resistance [°C/W]	Abbreviations TME Thorms mechanical fatigue		
\widetilde{s}	Deviator stress [Pa]	TMF	Thermo-mechanical fatigue	
α	Back stress for Chaboche model [Pa]	EV	Electric vehicle	
Y	Size of yield surface [-]	DC	Direct current	
C_i	Chaboche parameter [Pa]	AC	Alternating current	
γ_i	Chaboche parameter [-]	WBG	Wide band-gap	
$\widehat{arepsilon}^P$	Accumulated plastic strain [-]	SiC	Silicon carbide	
Δλ	Plastic multiplier [-]	Si	Silicon	
$\overline{\sigma}$	Equivalent stress against steady plastic flow [Pa]	GaN	Gallium nitride	
S	Deformation resistance [Pa]	Ga_2O_3	Gallium oxide	
С	Function of the temperature and strain rate[-]	DBC	Direct bonded copper	
$\dot{\epsilon}^P$	Inelastic strain rate [s ⁻¹]	IMC	Intermetallic compound	
5	Materials constant value [-]	PCT	Power cycling test	
Q	Activation energy [J]	IGBT	Insulated gate bipolar transistors	
A A	Pre-exponential factor [s ⁻¹]	ENIG	Electroless Nickel immersion Gold	
R	Universal gas constant [-]	AMB	Active metal brazing	
m	Strain sensitivity [-]	DSC	Double side cooling	
h_0	hardening/softening constant [-]	AlN	Aluminum nitride	
à	Strain rate sensitivity of hardening/softening [-]	Al_2O_3	Alumina	
s*	Saturation value [Pa]	$\mathrm{Si}_{3}\mathrm{N}_{4}$	Silicon nitride	
	strain rate sensitivity for the saturation value of	EOL	End-of-life	
n	deformation resistance [-]	SAT	Scanning acoustic tomography	
ŝ		EBSD	Electron backscatter diffraction	
	Anand coefficient [-]	HAGB	High angle grain boundary	
Hv	Hardness [H _v]	LAGB	Low angle grain boundary	
$\stackrel{H_0}{\sim}$	Intrinsic hardness resisting dislocation motion[H _v]	KAM	Kernel average misorientation	
k	material dependent strengthening coefficient [-]	GOS	Grain orientation spread	
k	Thermal conductivity [Wm ⁻¹ K ⁻¹]	IQ	Image quality	
0	Density [kg·m ⁻³]	CSL	Coincidence site lattice	
E	Young's modulus [GPa]	FEM	Finite element method	
ν	Poisson's ratio [-]	EMC	Epoxy molding compound	
C_p	Specific heat [Jkg ⁻¹ °C ⁻¹]	CTE	Coefficient of thermal expansion	
U	Strain energy [J]	DMM	Deformation mechanism map	
V	Volume [m ³]			

results of the previous studies clearly indicated that high-purity Cu experienced TMF-induced degradation below the recrystallization temperature [15]. Nevertheless, this was the result of a tensile test, and to apply it to power modules for automobiles, a study on driving PCT below the recrystallization temperature (i.e., below 250 °C) by applying pure Cu in the form of a clip to the power module has to be carried out fundamentally because the experience of applying the bare Cu clip to actual products and demonstrating it is industrially required. In the past, although there have been many reports of studies applying Cu clip bonding, most of the studies focused on solder degradations and intermetallic compounds. [19–21]. Even if the research was conducted under similar conditions, the focus of the main research was solder and wire interconnection, and no attention was paid to the microstructure of Cu. In particular, as far as the authors know, there is no literature on applying the Cu clip to the power module, performing PCT, and investigating the microstructure of the Cu clip in detail. The reason for this is that in the past, typical silicon (Si)-based power semiconductors were mainly applied to power conversion systems, but nowadays we introduce wide band-gap (WBG) power semiconductors (e.g., SiC, GaN, Ga₂O₃, etc.) to further miniaturize devices, achieve higher powers, and higher temperature operations [22,23]. As power semiconductors that

guarantee an operating temperature of over 200 °C begin to be massproduced, recently Cu, which had sufficient heat resistance to operate Si-based power semiconductors, is gradually being pointed out as a reliability problem in the automotive industry. Namely, in the past, since the power or operating temperature (T $_{imax}$ below 150 $^{\circ}\text{C})$ that was pursued was significantly lower than now, the most vulnerable part from that point of view was the solder joints and related intermetallic compound (IMC) layers. The excellent conductivity and high melting point of Cu components operating at low operating temperatures have made it difficult for researchers who handled electronics to view them as a weakness. Now, as higher operating temperatures (T_{imax} beyond 175 $^{\circ}$ C) and durability are gradually becoming spotlight as specifications, durability issues of the Cu components. Therefore, an in-depth understanding of the power cycling behavior of the Cu clip considering all of the Cu clip - solder material - DBC substrate - power device - EMC at the new generation power module scale is an industrially urgent task.

In this study, to prove the power cycling durability of bare Cu clip wires, we applied a Cu clip to a transfer-mold type power module for applications in electric vehicles (EVs) and conducted power cycling tests (PCT). Changes in thermal resistance, which determine the lifetime of power modules, were monitored up to failure stages, and

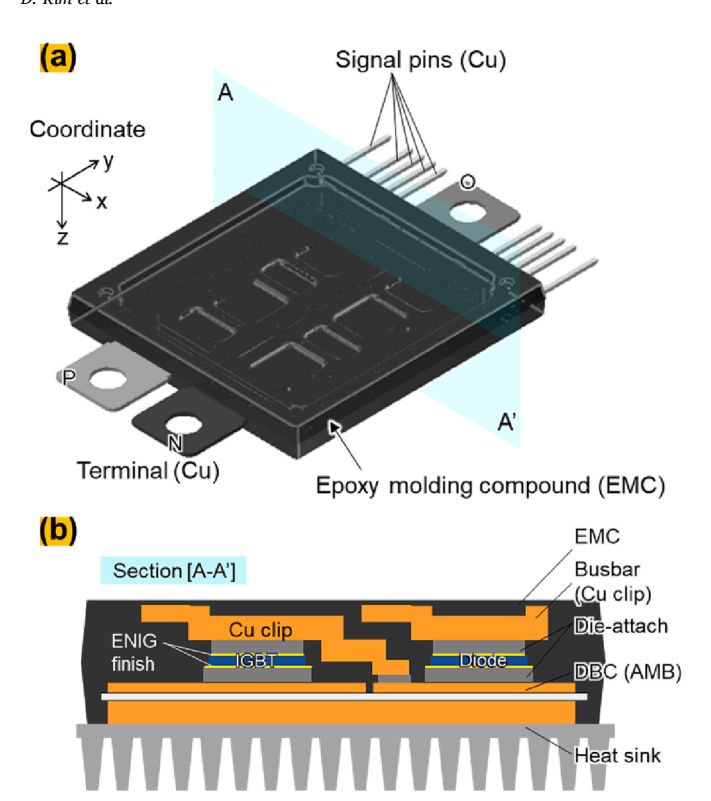


Fig. 1. Descriptions of a Cu clip bonded transfer molded power module. (a) 3D design model and (b) component configuration of the power module structure.

Si

■EMC

Table 1The applied condition of active power cycling tests.

	t _{on} /t _{off} (sec)	I _{load} (A)	T _c (°C)	T _{jmax} (°C)	Δ T _j (°C)	Coolant (LPM)	_
		550	50	175	125	12	
Cond.	0.5/ 4.5						

crystallographic degradations of bare Cu clip wiring were systematically investigated. The structure of this thesis is as follows: Chapter 1 is the introduction, Chapter 2 describes the materials and methods introduced in this study in detail, Chapter 3 discusses the experimental results, and Chapter 4 discusses the mechanism using numerical simulation in detail. This work focuses on how bare Cu clip wire interconnections behave mechanically and microstructurally in the power module structure by PCTs.

2. Materials and methods

2.1. Power cycling test

Fig. 1(a) and (b) illustrate 3D modeling and components of the Cu clip bonded transfer-mold type power module. The power module is fabricated with four EA Si insulated gate bipolar transistors (IGBTs) and four EA Si diodes with high and low sides. The IGBT die size is 120 mm², while the diode die size is 63 mm². Both IGBT and diode Si dies were metalized with electroless Ni/immersion Au (ENIG) finishes on the top and back sides, which were bonded onto an active metal brazed (AMB) aluminum nitride (AIN)-DBC substrate using a preform type solder

material, respectively. Pure copper (purity 99.99%) was introduced as a Cu clip bonding. Finally, the power module was molded through the transfer molding process and the pins were trimmed.

A condition of the active power cycling test is shown in Table 1, ON switching for 0.5 s and OFF switching for 4.5 s, a total of 5 s corresponding to 1 cycle. The heat distribution and their switching configuration by the power cycling operation of the power module were visualized as shown in Fig. 2(a). Then, the maximum junction temperature (T_{imax}) is to be 175 °C at Si diodes (i.e., T_{imax} is based on the Si die, and R_{th} is also measured based on the T_{imax} of the Si die.). Obviously, T_{imax} occurs from the Si die and dissipates the heat loss from the Si die through the heatsink and Cu clips in this system. And the temperature of the heat sink (T_c) is sustained by 50 °C (see Fig. 2(b)). T_c is monitored by a thermocouple (TC) attached to the water cooling system. Under this condition, it is operated until failure (constant ΔT_i mode). The end-oflife (EOL) of PCs is referred from European Center for Power Electronics (ECPE) guideline AQG-324. The change from the standard value defines forward voltage + 5% and thermal resistance + 20% as failure criteria. The temperature difference ΔT between the maximum junction temperature (T_{imax}) of the Si die and case temperature: heat sink temperature (T_c) is caused by theoretical thermal resistance and power dissipation in the vertical direction. In this study, ΔT is sustained by 125 °C, which can be expressed by

$$\Delta T = T_{imax} - T_c = P_D \times R_{th} \tag{1}$$

where P_D denotes the power dissipation of power devices (i.e., Si die), T_{jmax} is the maxmum junction temperature of the Si die, T_c denotes the heat sink temperature, and R_{th} is the thermal resistance, thus, the thermal resistance can be calculated as:

$$R_{th} = \frac{T_{jmax} - T_c}{P_D} \tag{2}$$

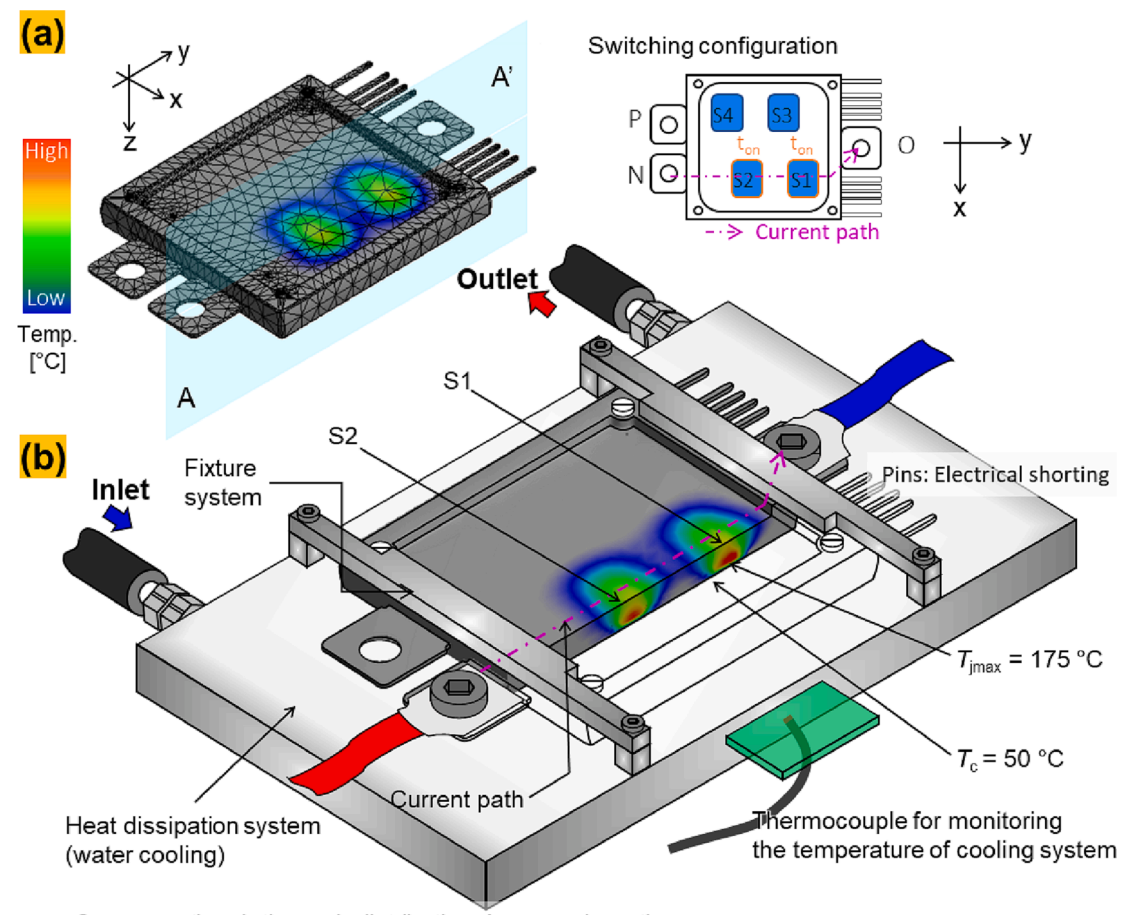
based on Eqs (1) and (2), the thermal resistance was measured in real time in this study.

2.2. Materials characterization

Non-destructive testing was performed using scanning acoustic tomography (SAT) to seek the origin cause of the failure due to the increase in thermal resistance by PCTs. Here, the defect portions are identified by white area. For the quantitative microstructural analysis, the specimens were cold mounted using epoxy resin at room temperature (RT) for 48 h, then the cross-section of each cycle was cut, mechanically polished up to grade 4,000 SiC sandpaper, and then polished up to 1 µm (Struers/DP-Suspension P and OP-S). Finally, to obtain the mirror polished surface, a 0.04 µm aqueous solution containing colloidal silica particles was ultimately applied (Struers/OP-S). Then, the mechanically polished specimens were precision polished with an ionmilling machine (JEOL, IB-09020CP), which was processed with an acceleration voltage of 4.5 kV and an Ar + gas flow rate of 0.15 cm³/ min. The crystallographic quantitative analysis of the Cu clip joint area was performed through an electron backscattered diffraction (EBSD, Velocity Super, EDAX, USA) detector. For the detail, the EBSD scanning condition was that the magnification was x200, the scan step was 0.75, and the total scanning was 985,908 points. TSL-OIM software was used to analyze crystallographic raw data from EBSD in detail; analysis points with a confidence index (CI) of 0.1 were indicated as black regions. Vickers hardness depending on the power cycling was measured for the Cu clip with a micro-Vickers hardness testing machine (HM-200 Autovick, Mitsutoyo, Japan).

2.3. Numerical material models for power cycling

In this study, the Chaboche model includes kinematic hardening, which can account for the observed hardening effect in Cu with increasing active cycles in simulations, even in the absence of isotropic



Cross sectional thermal distribution image when the power module is ON switching; The difference in the thermal behavior of S1 and S2 appears, and the heat transfer path can be seen in the simulated result.

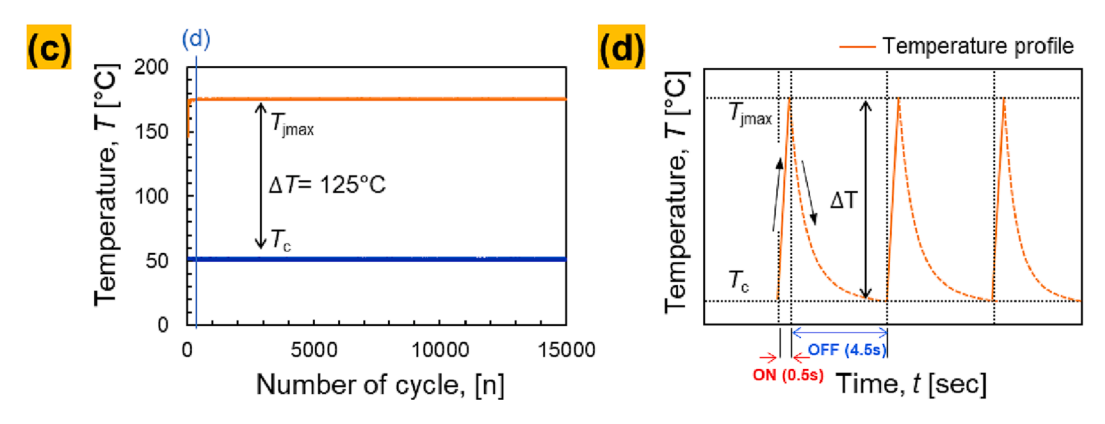


Fig. 2. (a) schematic descriptions of thermal distributions when the power ON state, (b) descriptions of sections A-A' in (a), which included the layout description of the connection and layout relationship between the Cu clip-bonded transfer molded power module and the test equipment in detail, (c) a temperature history during the power cycling test and (d) a schematic description of temperature behavior in detail during PCTs.

Table 2 Parameters for Chaboche constitutive model of pure Cu.

Temperature (°C)	C ₁ (MPa)	γ_1	C ₂ (MPa)	γ_2
20	54,041	962	721	1.1
50	52,880	1,000	700	1.1
150	45,760	1,100	600	1.1
250	38,040	1,300	400	10

hardening. In a previous study [24], a predominant kinematic hardening was experimentally observed and modelled with a Chaboche-based hardening model in the majority of Cu cases. In addition, this model has been used as a model that can satisfactorily explain the nonlinear kinematic hardening for the elastic–plastic deformation behavior by considering the temperature effect of the copper [25,26]. In previous studies, the experimental nature of this material and the compatibility of the Chaboche material model have been well established [24]. Kinematic hardening reflects the contribution of the previous loading history

Table 3Anand visco-plasticity parameters of solder preform A.

Material parameters	
A (sec ⁻¹)	993
Q/R (K)	4461
ξ	5.6
m	0.3959
<i>š</i>	78.4
$h_0(MPa)$	77,930
à	1.1
<i>s</i> ₀	1.56

to the current stress–strain behavior and can arise from mechanisms such as dislocation rearrangement or the accumulation of internal stresses. For this reason, Chaboche constitutive model with non-linear kinematic hardening, which took the temperature effect into account and fit cyclic thermal loading well, was used to express the elastic—plastic behavior of the pure copper. The yield function for the Chaboche [25] nonlinear kinematic hardening rule is written as:

$$f(\sigma - \alpha, Y) = \sqrt{\frac{3}{2}(\widetilde{s} - \alpha)}(\widetilde{s} - \alpha) - Y = 0$$
(3)

where \tilde{s} is the deviator stress, α denotes the back stress for the Chaboche model describing the kinematic hardening rate, and $Y = \sqrt{2/3}\sigma_0$ refers to the size of yield surface which will be constant in a kinematic hardening model. The back stress, α can be expressed by

$$\alpha = \sum_{i=1}^{n} \alpha_i \tag{4}$$

The nonlinear hardening rules of Chaboche is as follow:

$$\Delta \alpha_i = \frac{2}{3} C_i^* \Delta \varepsilon^P - \gamma_i \alpha_i^* \Delta \widehat{\varepsilon}^P + \frac{1}{C_i} \frac{dC_i}{d\theta} \Delta T^* \alpha$$
 (5)

where C_i and γ_i respectively represent the Chaboche material parameters, respectively. C_i is initial hardening modulus and γ_i controls the decreasing rate of hardening modulus with increasing plastic strain, and i is the number of kinematic models. ΔT is the temperature and $\hat{\epsilon}^p$ represents the accumulated plastic strain. The flow rule establishes the direction of the plastic flow. The plastic strain increments will be in the direction of the yield surface gradient, assuming an associated:

$$\Delta \varepsilon^{P} = \Delta \lambda \frac{\partial f}{\partial \sigma} = \Delta \lambda \frac{s - a}{\sqrt{2J_{\gamma}}} \tag{6}$$

where $\Delta\lambda$ denotes the plastic multiplier and is determined by the consistency condition and $\sqrt{2J_2} = \sqrt{(s-a)(s-a)}$. The Chaboche parameters applied in this study are shown in Table 2[25].

In general, it is well known that a metallic alloy including solder alloy has a creep behavior which is exposure at the thermomechanical environments above half the melting point e.g., thermal cycling, power cycling, and temperature aging [27–30]. Herein we examine whether the solder creep behavior occurs during PCTs, and we focus on whether it can significantly affect the deformation of the Cu clip and the entire power module structure. The solder introduced in this study was assumed to have a thermomechanical response with the Anand viscoplastic constitutive model. The model can be written as [31]:

$$\overline{\sigma} = cs$$
 (7)

where $\overline{\sigma}$ is an equivalent stress against the steady plastic flow, and s is a deformation resistance (i.e., internal valuable) with the dimensions of stress, c is a function of the temperature and strain rate, which is expressed by

$$c = c(\dot{\varepsilon}^P, T) = \frac{1}{\xi} sinh^{-1} \left[\frac{\dot{\varepsilon}^P}{A} exp\left(\frac{Q}{RT}\right) \right]^m$$
 (8)

here, T is the temperature, R is the universal gas constant, ξ is the materials constant value, the $\dot{\varepsilon}^P$ is the inelastic strain rate, A is the pre-exponential factor, and Q is the activation energy, m is the strain sensitivity. Substituting Eq (7) into Eq (8), the stress equation can be expressed as:

$$\overline{\sigma} = \frac{s}{\xi} \sinh^{-1} \left[\frac{\dot{\varepsilon}^P}{A} exp\left(\frac{Q}{RT}\right) \right]^m \tag{9}$$

The flowing functional form for the flow equation of the Anand model was utilized to exactly accommodate the strain rate dependence on the stress at the constant structure [32], rearranging Eq (9) and solving for the strain rate yields the flow equation of the Anand model:

$$\dot{\varepsilon}^{P} = A \exp\left(-\frac{Q}{RT}\right) \left[\sinh\left(\xi\frac{\overline{\sigma}}{s}\right)\right]^{\frac{1}{m}} \tag{10}$$

moreover, the evolution equation for the deformation resistance with the dimensions of stress, \dot{s} is assumed given by

$$\dot{s} = h(\overline{\sigma}, s, T)\dot{\varepsilon}^P \tag{11}$$

where

$$h = h_0 \left| 1 - \frac{s}{s^*} \right|^{\dot{a}} sign \left(1 - \frac{s}{s^*} \right) \dot{a} > 1$$
 (12)

combining Eqs. (11) and (12), the evolution equation for the internal variable (i.e., deformation resistance) \dot{s} is derived as:

$$\dot{s} = \left\{ h_0 \left| 1 - \frac{s}{s^*} \right|^{\dot{a}} sign\left(1 - \frac{s}{s^*} \right) \right\} \dot{\varepsilon}^P$$
 (13)

where s^* describes the saturation value of s associated with a set of given temperature and strain rate, which can be derived as follow:

$$s^* = \hat{s} \left[\frac{\dot{\varepsilon}^P}{A} exp\left(\frac{Q}{RT}\right) \right]^n \tag{14}$$

where h_0 is the hardening/softening constant, \dot{a} denotes the strain rate sensitivity of hardening/softening, n is the strain rate sensitivity for the saturation value of deformation resistance, and \hat{s} is the coefficient, respectively. For $s < s^*$, Eq (12) can be rewritten as follows [33]:

$$ds = h_0 \left(1 - \frac{s}{s^*} \right)^a d\varepsilon^P \tag{15}$$

and then integrated to yield as

$$s = s^* - \left[(s^* - s_0)^{1 - \dot{a}} + (\dot{a} - 1) \left\{ (h_0)(s^*)^{-\dot{a}} \right\} \varepsilon^P \right]^{\frac{1}{1 - \dot{a}}}$$
 (16)

where $s(0) = s_0$ is the initial value of s at time t = 0. Substituting Eq (14) into Eq (16) yields the final version of the evolution equation for the internal variable (deformation resistance) s:

$$s = \hat{s} \left[\frac{\dot{\varepsilon}^{P}}{A} exp\left(\frac{Q}{RT}\right) \right]^{n} - \left[\left[\hat{s} \left[\frac{\dot{\varepsilon}^{P}}{A} exp\left(\frac{Q}{RT}\right) \right]^{n} - s_{0} \right]^{1-\dot{a}} + (\dot{a} - 1) \left\{ (h_{0}) \left(\hat{s} \left[\frac{\dot{\varepsilon}^{P}}{A} exp\left(\frac{Q}{RT}\right) \right]^{n} \right)^{-\dot{a}} \right\} \varepsilon^{P} \right]^{\frac{1}{1-\dot{a}}} (17)$$

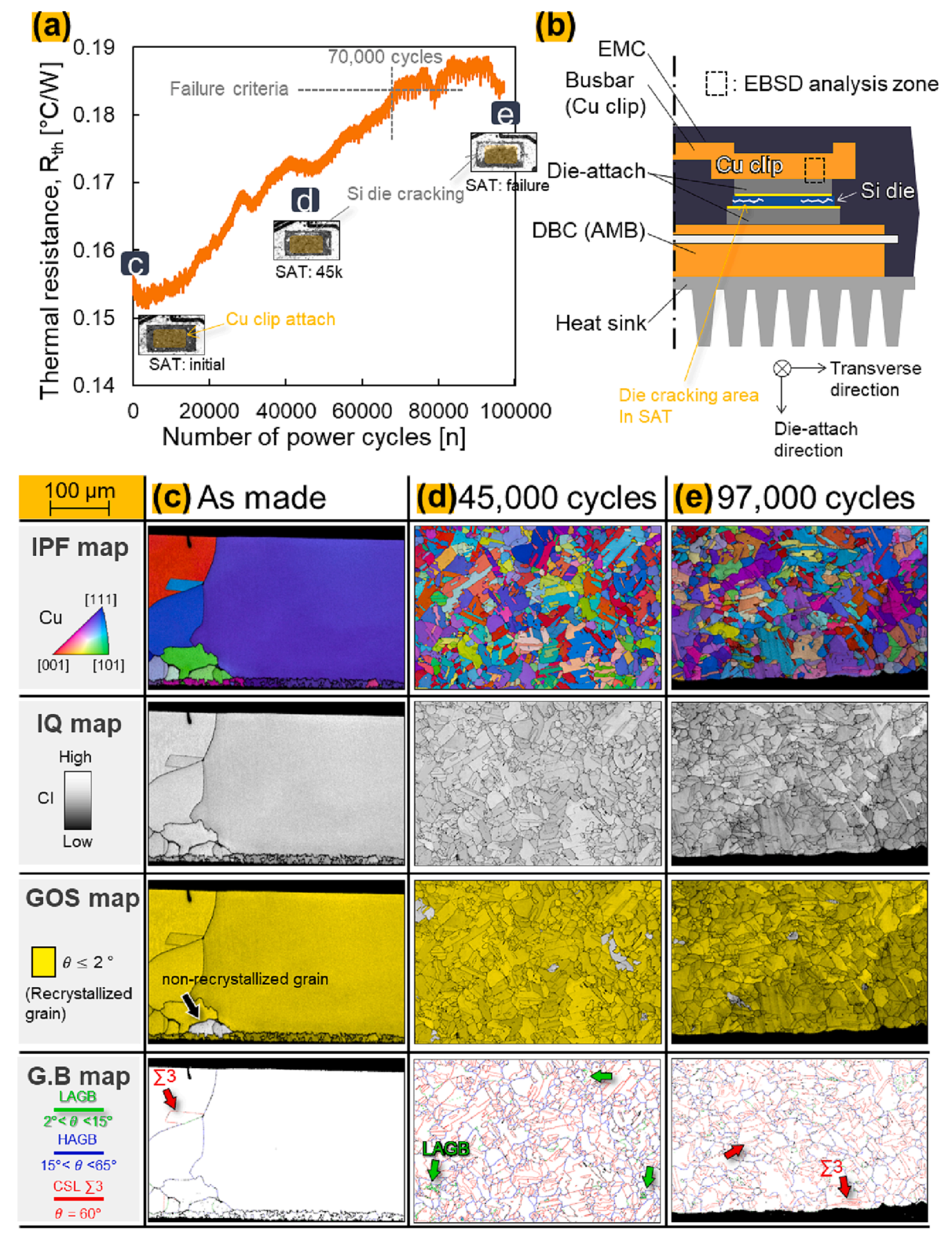


Fig. 3. Results of the power cycling tests and change of Cu clip microstructures. (a) measurement results of the thermal resistance and defect change results by scanning acoustic tomography, (b) schematic description of EBSD observation area and the defect location, and (c) EBSD analysis result of initial state, (d) 45,000 cycles, (e) 97,000 cycles. GS: grain size; IPF: inverse pole figure; IQ: image quality; GOS: grain orientation spread; G.B: grain boundary.

or
$$s = s\left(\dot{\varepsilon}^{P}, \, \varepsilon^{P}\right) \tag{18}$$

The final equations in the Anand model are the stress equation in Eq. (9), the flow equation in Eq. (10), and the integrated evolution equation

in Eq (17). These expressions include 9 material parameters (constants). Theoretical Formulation for Uniaxial Stress-Strain response the post yield uniaxial stress–strain relations predicted by the Anand model are obtained by substituting the expression for internal variable s from Eq (17) into the stress equation in Eq (9). The calculation results in:

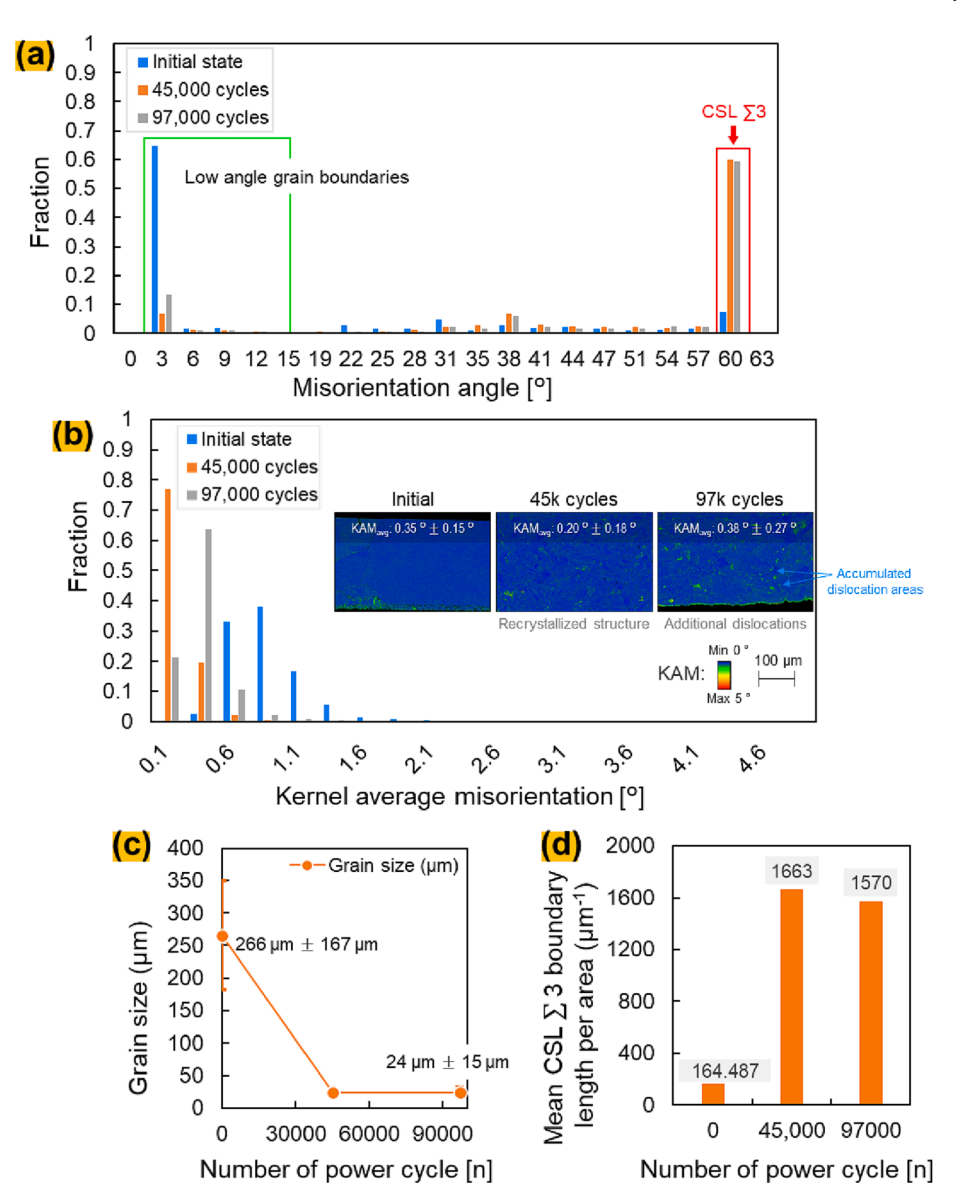


Fig. 4. Measurement results of Cu clip microstructures depending on power cycling. (a) Distribution plots of misorientation angle, (b) plots of kernel average misorientation angle, and (c) changes in grain size depending on power cycles, (d) mean CSL $\sum 3$ boundary length per measurement area.

$$\overline{\sigma} = \frac{1}{\xi} \sinh^{-1} \left[\frac{\dot{\varepsilon}^P}{A} exp \left(\frac{Q}{RT} \right) \right]^n \left[\widehat{s} \left[\frac{\dot{\varepsilon}^P}{A} exp \left(\frac{Q}{RT} \right) \right]^n - \left[\left[\widehat{s} \left[\frac{\dot{\varepsilon}^P}{A} exp \left(\frac{Q}{RT} \right) \right]^n - s_0 \right]^{1-\dot{a}} + (\dot{a} - 1) \left\{ (h_0) \left(\widehat{s} \left[\frac{\dot{\varepsilon}^P}{A} exp \left(\frac{Q}{RT} \right) \right]^n \right)^{-\dot{a}} \right\} \varepsilon^P \right]^{\frac{1}{1-\dot{a}}} \right] (19)$$

namely, as follows:

$$\overline{\sigma} = \overline{\sigma} \left(\dot{\varepsilon}^P, \, \varepsilon^P \right) \tag{20}$$

For a uniaxial tensile test performed at fixed (constant) strain rate and constant temperature *T*, this expression represents highly nonlinear stress–strain behavior (power law type function) after yielding:

$$\overline{\sigma} = \overline{\sigma} \left(\varepsilon^P \right) \tag{21}$$

the Anand model predictions for the yield stress (σ_Y) and the ultimate tensile strength (i.e., UTS = maximum/saturation stress) can be

obtained by considering limiting cases of Eq (20). The limit gives the UTS as ε^P goes to ∞ :

$$UTS = \overline{\sigma}|_{\varepsilon^{P} \to \infty} = \frac{\widehat{s}}{\xi} \left[\frac{\dot{\varepsilon}^{P}}{A} exp\left(\frac{Q}{RT}\right) \right]^{n} sinh^{-1} \left[\frac{\dot{\varepsilon}^{P}}{A} exp\left(\frac{Q}{RT}\right) \right]^{m} \equiv \sigma^{*}$$
 (22)

while the σ_Y is given by the limit as ε^P goes to 0:

$$\sigma_{Y} = \overline{\sigma}|_{\varepsilon^{P} \to 0} = cs_{0} = \frac{1}{\xi} \sinh^{-1} \left\{ \left[\frac{\dot{\varepsilon}^{P}}{A} exp\left(\frac{Q}{RT}\right) \right]^{m} \right\} s_{0} \equiv \sigma_{0}$$
 (23)

Hence, using the saturation stress ($\sigma^* = \text{UTS}$) relation in Eq (22), the post yield stress–strain response in Eq (21) can be rewritten by

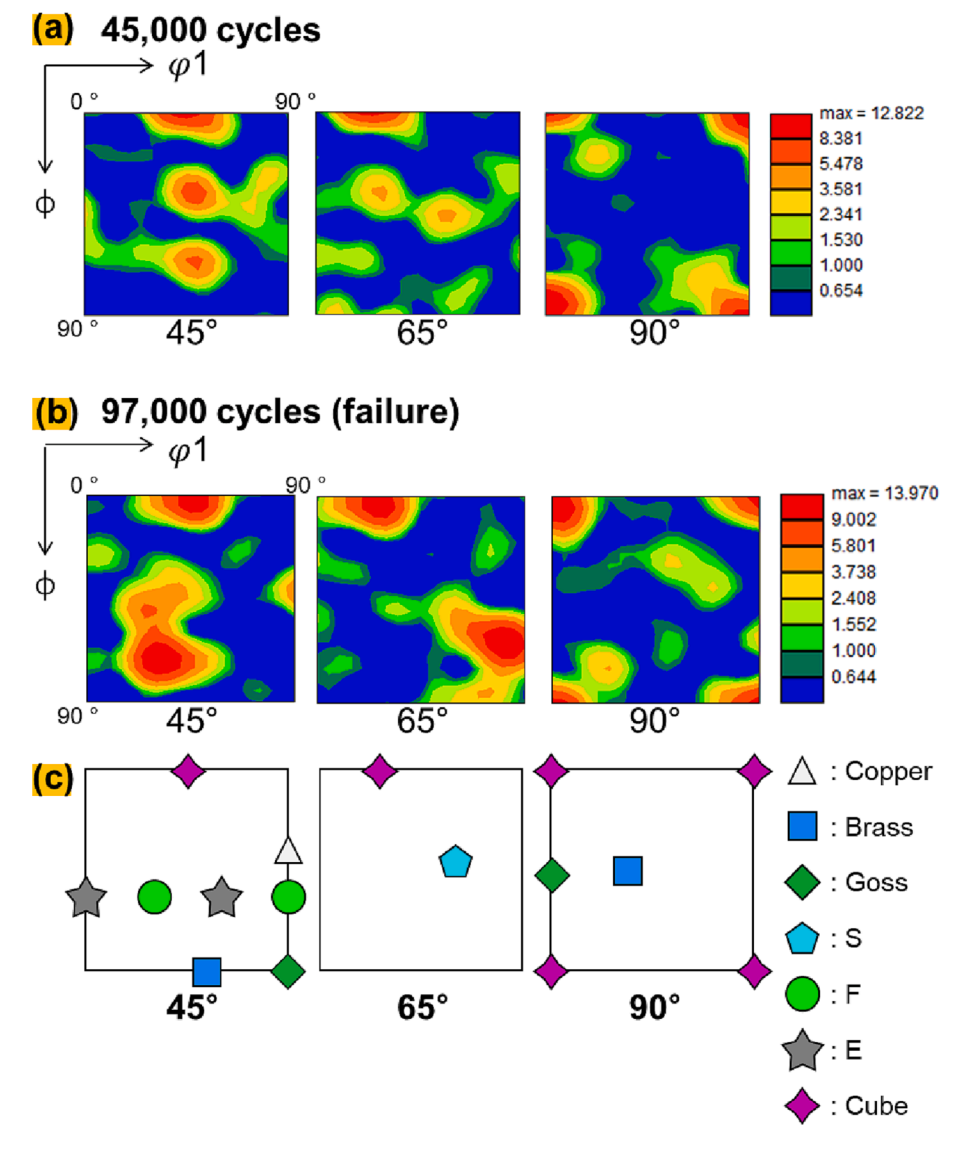


Fig. 5. Texture developments of Cu clips depending on the power cycling test. (a) 45,000 cycles, (b) 97,000 cycles, and (c) ideal texture maps for face-centered cubic structures.

Table 4 Ideal texture components.

Texture component	$\{hkl\} < uvw>$	$\varphi_1 [^\circ]$	ф[°]	$\varphi_2[^\circ]$
Copper	{112} (111)	90	35	45
Brass	{011} (211)	35	45	0
Goss	$\{011\}\ \langle 100\rangle$	0	45	0
S	{123} (634)	59	37	63
F	$\{111\}\ \langle 112\rangle$	30/90	55	45
E	$\{111\}\ \langle 001 \rangle$	0/60	74	45
Cube	$\{001\}\ \langle 100\rangle$	0	0	0

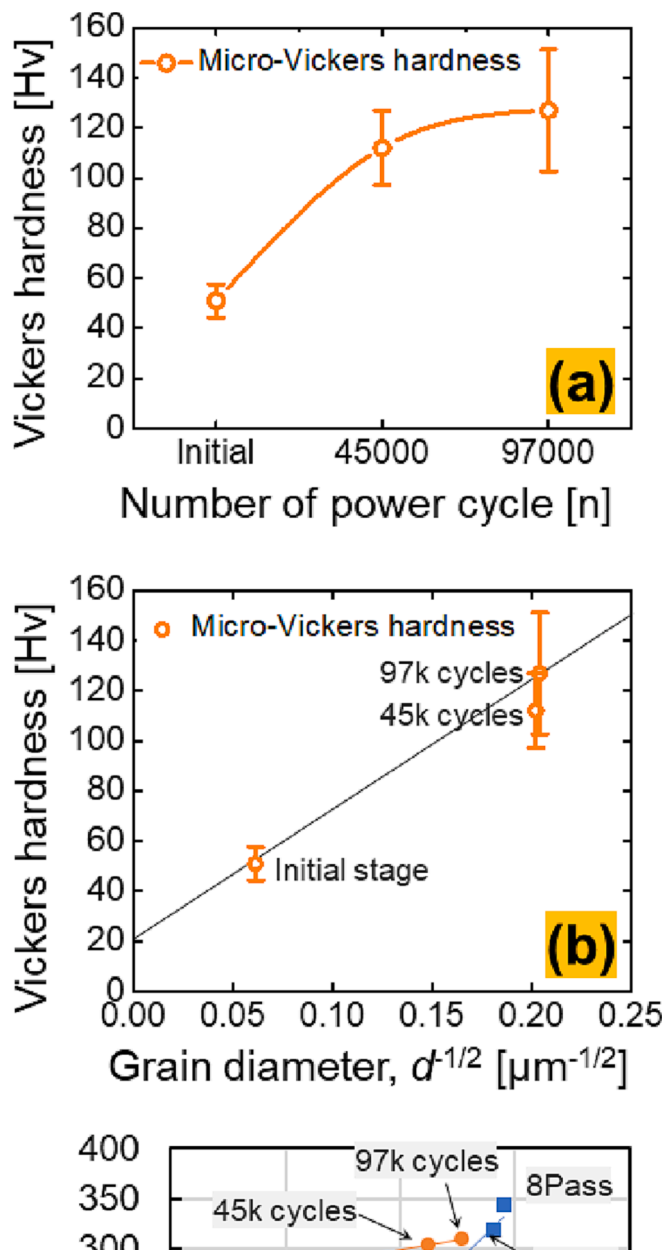
$$\overline{\sigma} = \sigma^* - \left[(\sigma^* - cs_0)^{1-\dot{a}} + (\dot{a} - 1)\{(ch_0)(\sigma^*)^{-a}\}\dot{\varepsilon}^P \right]^{\frac{1}{1-\dot{a}}}$$
 (24)

in here, values of the material parameters of Q/R, A, h_0 , \hat{s} , $s_0 \xi$, \dot{a} , m. where $\sigma_0 = cs_0$ and s_0 is the initial value of s. The non-linear parameters of the solder preform A are displayed in Table 3.

3. Results

3.1. Power cycling durability

Thermo-mechanical fatigue is a physical phenomenon experienced by a power module during a power cycling test, which causes a fundamental failure of the power module. Mainly, the reduction of the durability in power modules is caused by solder joint cracks, lift-off of wire bonding, and heel cracking, resulting in thermal resistance increase or rapid increase in current and voltage. Fig. 3(a) represents the result of thermal resistance measurement depending on power cycles. The thermal resistance of the as-made Cu clip bonded power module was about $0.155\,^{\circ}$ C/W, and it reached about $0.17\,^{\circ}$ C/W at 45,000 cycles. When the power cycling reached 70,000 cycles, a failure corresponding to the thermal resistance + 20% compared to the initial occurred. This is a distinct failure mode from wire bonding type power modules, which mainly cause + 5% of V_{ce} and runaway failures based on lift-off or heel cracking of the wire bonding region [34]. The leading cause of failure was Si die cracking propagation, as shown in the SAT observation results. The gradual increase in thermal resistance and the extensibility of deficiencies identified in the SAT (white areas) are characterized by linear trends. Fig. 3(b) illustrates a schematic description of the



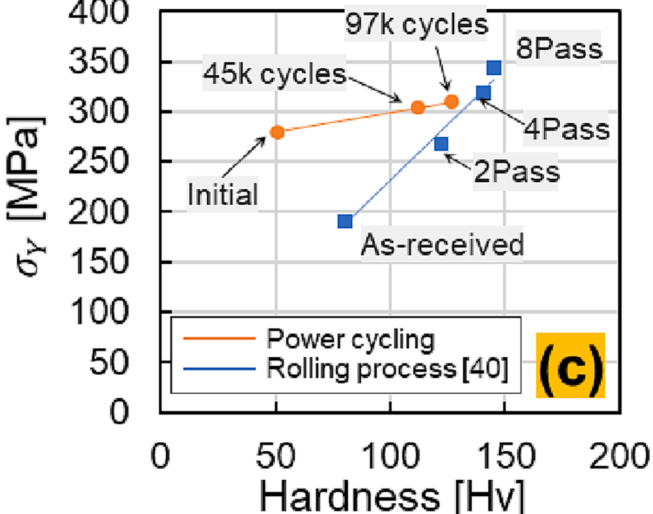


Fig. 6. (a) Vickers micro hardness change depending on power cycles, (b) Hall-Petch relation plot, and (c) theoretically calculated yield strength: Hardness - yield stress relationship correlation between power cycling test and rolling process [40]. orange color: this study; skyblue color: rolling process; σ_Y : yield stress.

locations of defects identified on the SAT and areas of EBSD analysis. In addition, the change in the crystallographic properties of the Cu clip subjected to repeated thermo-mechanical fatigue by power cycling is quantitatively considered in the next section.

3.2. Microstructural changes of Cu clip

The microstructure of the Cu clip also underwent significant changes while the thermal resistance increased by power cycling tests. Fig. 3(c-e) depicts crystallographic characteristics of Cu clip wires changed during PCTs by EBSD observation. The grain size of the Cu clip immediately after soldering and EMC molding was about 266 μm , and it had the grain characteristics of complete recrystallization (see Fig. 3(c)). In the Cu clip subjected to 45,000 cycles of PCTs, a substantial decrease in the grain size was observed to about 24 µm, and the grain orientation was randomly distributed as displayed in Fig. 3(d). As seen in the grain boundary (G.B.) maps, it can be seen that the fraction of $\sum 3$ twin boundaries significantly increased, and low angle grain boundaries (LAGBs) were also observed. Previous research results have been reported that an increase in the fraction of $\sum 3$ twin boundaries in highpurity Cu directly affects the increase in fatigue strength [15]. In Fig. 3(e), the grain size of the specimen that reached failure (97,000 cycles) was also found to be about 24 µm. As can be seen from the image quality (IQ) map, grains darker than 45,000 were seen, which can be considered to be due to the accumulation of dislocations due to repetitive heat from PCTs. Grain orientation spread (GOS) maps represent that were found that grain boundaries of less than 2 $^{\circ}$ exist inside most of the grains, and it is considered that fully recrystallized grains without subgrain boundaries occupied the microstructure of the Cu clip. In addition, the copper grain size has an impact on the warpage and lifetime of substrates. From the previous study result, repetitive thermal behavior investigations have shown that degradations appear first on DBC substrates with fine copper grain size [10]. Importantly, crystalline imperfections known as dislocations can easily move throughout the crystalline grains but grain boundaries stop dislocations. Smaller grains have a greater ratio of surface area to volume, which means a greater ratio of grain boundary to dislocations. Namely, the more grain boundaries exist, the higher the deformation resistance and strength due to the grain boundary suppressing the dislocation moving. As seen in the IQ maps in Fig. 3, more dark areas can be identified at 97,000 cycles, which clearly indicates that the grain size has reached a steady state compared to 45,000 cycles, but the accumulation of dislocations by PCTs is remarkable. In this context, one of the possibilities is that the material has reached a steady state where the grain size reduction due to power cycling is balanced by the grain growth mechanisms, resulting in a stable grain size. This possibility can also be reasonably estimated from the trend of hardness change of copper undergoing repeated heating from previous studies [10].

Fig. 4 summarizes the graph plotting for measured results of the Cu clip microstructures. The fraction of LAGBs with a misorientation angle of less than 15 ° had a tendency to significantly decrease from about 0.65 in the initial state to less than 0.2 after the power cycling tests as shown in Fig. 4(a). In contrast, coincidence site lattice (CSL) $\sum 3$ boundaries were dramatically increased as the LAGB decreased, and most of the grain boundaries after PC tests were formed as $\sum 3$ boundaries (refer to fig for the change of mean CSL boundary length per area according to power cycling). In Fig. 4(b), the kernel average misorientation (KAM) angle plot represents no significant difference, and a slight increase was seen until failure after 45,000 cycles. However, as power cycling progressed, relatively high KAM values were distributed to the grain boundaries, and as power cycling continued, higher KAM values were distributed to the internal of the grain. This is regarded as the introduction of dislocations of the Cu clip by power cycling - resolutions of dislocations by recrystallizations - grain change- accumulation of dislocations. It is considered that after the critical cycles region, the change in grain size reaches a steady state, and there is no significant change,

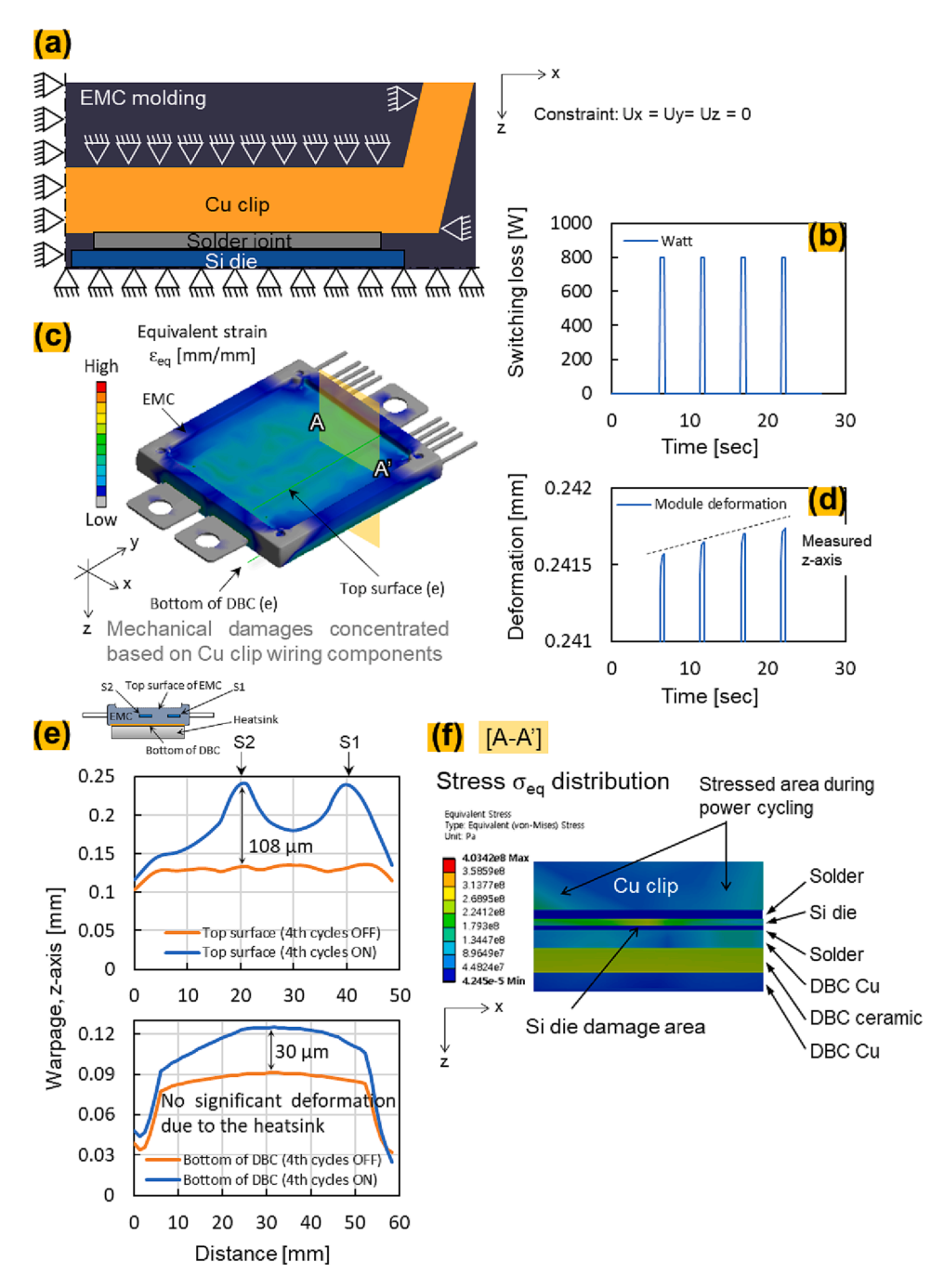


Fig. 7. (a) Geometrical constraint of the Cu clip during power cycles, (b) applied power loss profile as a boundary condition, (c) the map of the simulated strain distribution, and (d) deformation dependence of power cycling corresponding to the input switching loss, (e) the warpage deformation at the top surface of EMC and bottom of DBC substrate, (f) a cross sectional stress distribution of power module structure.

Table 5Applied material properties for simulation.

	Density,ρ (kg/m³)	CTE, a (ppm)	Specific heat, C_p (Jkg ^{-1o} C $^{-1}$)	Thermal conductivity, k (W/mK)	Elastic modulus, E (GPa)	Poisson's ratio (-)
Si	2307	2.6	794	129	130	0.3
Cu	8903	17	386.4	424.5	119.75	0.34
Solder preform A	7400	21.7	231	64.2	54.2	0.35
AlN	3260	4.5	740	70–250	330	0.24
EMC	1000	130	120	0.5	1	0.4

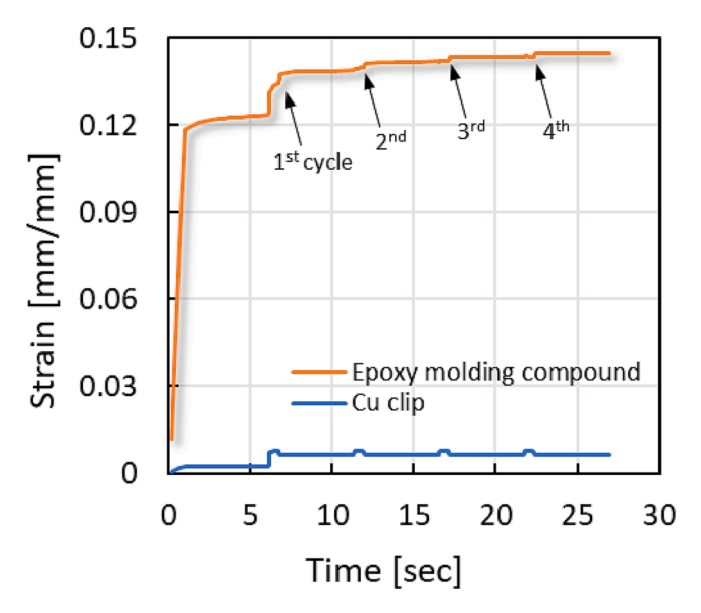


Fig. 8. a Plot of strain behaviors of epoxy molding compound and Cu clip.

and dislocations are accumulated only by repeated PCTs. Fig. 4(c) summarizes the changes in grain size, repetitive power cycling reduced the grain size of the Cu clip to 90%. As the grain size was refined, the change in the density of the twin boundaries is shown in Fig. 4(d). As the concentration of Cu increases in a CSL \sum 3 boundary, the density of the boundary increases, which means that more boundary sites are present in a given area. This leads to an increase in the boundary's resistance to deformation and thus an improvement in its mechanical strength. In particular, this twin boundary density result can directly prove that repeated PCTs can make the Cu clip more rigid (i.e., hardening).

The Cu clip that was subjected PCTs showed remarkable texture developments as displayed in Fig. 5. Ideal texture components are shown in Table 4. The Cu clip that has undergone 45,000 cycles was a noticeable development of the cube texture (see Fig. 5(a)). The development of the Cube component has been reported that cold-rolled pure Cu sheets [35]. This means that the Cube component can be developed when a load was generated below the recrystallization temperature. Namely, this behavior can be derived that the stress experienced by the Cu clip during power cycling may be a stress corresponding to the cold rolling process. In Fig. 5(b), the Cu clip texture in the failure state developed a stronger Cube texture similar to 45,000 cycles, but the development of copper texture is also noteworthy. This means that the repetitive thermo-mechanical fatigue behavior by PCTs directly affects the texture component development of Cu wires. The texture map that can be developed in face-centered cubic (FCC) metal is shown in Fig. 5 (c). The mechanism for the development of cube texture is covered in more detail with FEM simulation in the discussion section.

3.3. Micro-Vickers hardness of Cu clips

In this section, a micro-Vickers hardness test was performed to verify that hardening of the Cu clip occurred that attributed to the crystallographic behavior when the number of power cycling was increased. Fig. 6(a) exhibits a correlation between the cycle number of PCTs and Vickers hardness. The microhardness of the Cu clip was about 51.4 Hv in the initial state, and the microhardness of the Cu clip after 45,000 cycles of PCT exceeded 112 Hv. The microhardness of the Cu clip that reached failure (97,000 cycles) was about 127 Hv, and as the number of power cycles increased, the microhardness of the Cu clip showed a tendency to gradually increase. Thus, the power cycling number-dependent micro-Vickers hardness change reveals notable results. These results suggest that the power cycling operation crystallographically changed the

microstructure of Cu clips, which can be a clear strain hardening cause of the increase in hardness. The accumulation of deformation and internal dislocations can increase the hardness, but hardness is highly related to grain refinement. This phenomenon is related to crystallographic characteristics including grain size. The increase in hardness/strength of polycrystalline metals with decreasing grain size, d, following a $d^{-1/2}$ relationship was first described by Hall [36] and Petch [37] in the early 1950s [38]:

$$H_{v} = H_{0} + \tilde{k} - d^{-1/2}$$
 (25)

where $H\nu$ is the hardness, H_0 is the intrinsic hardness resisting dislocation motion and \widetilde{k} is a material-dependent strengthening coefficient. As seen in Fig. 6(b), it can be seen that our results are in good agreement with the Hall-Petch relationship. Here, yield strength (σ_{γ}) is expressed as follows:

$$\sigma_Y = \sigma_0 + \widetilde{k} \cdot d^{-1/2}$$
 (26)

with the yield strength σ_0 for the start of dislocation movement, the strengthening coefficient \widetilde{k} - and the grain size d. The hardness is linearly dependent on the yield strength as [39]:

$$\sigma_Y = 0.385 * Hv - \Delta \sigma \tag{27}$$

where $\Delta \sigma$ is the increase in stress due to work hardening during deformation up to the characteristic strain. Thus, the calculated yield stress based on theoretical equations can be derived in Fig. 6(c). Here, the initial yield stress after module assembling of the Cu clip employed in this study is estimated to be about 280 MPa, the Cu clip that has undergone 45 k cycles was hardened to 304 MPa, and the yield stress in the failure state can be hardened to about 310 MPa. Hardness and yield strength also tended to increase linearly as the number of PCTs and passes of the rolling process gradually increased. Even, the hardness and yield strength of 45 k cycles and 97 k cycles are located in a region similar to Cu that has been work-hardened by repeated rolling several times. This demonstrates the remarkable enhancement of Hall-Petch reinforcement by strain hardening experienced by bare Cu clip wires during the power cycling tests. This is the discovery of the behavior of bare Cu, which was unexpected in the previously reported results. Therefore, this means that even if the DBC substrates are replaced with bare Cu plates, it is important to access the power module by carefully considering the combination with the semiconductor device and bonding material in consideration of the thermomechanical fatigue of the Cu materials.

4. Discussion

4.1. The power module subjected to thermomechanical fatigue

Above discussed results mean that when bare Cu is also constrained by Si die and solder joint, EMC molding, strain hardening can occur remarkably. This strain hardening means that as the number of power cycles increases, the Cu clip loses elasticity and is gradually plastically deformed, which may cause critical damage to the joint interfaces constituting the power module structure. To seek the origin of the strain hardening of the bare Cu clip wiring, the mechanical behavior of the power module was analyzed by using a three-dimensional (3D) finite element method (FEM) simulation. The details of the geometric boundary conditions experienced by the Cu clip are shown in Fig. 7(a). This is a detailed view of the Cu clip, and the heat sink system is attached to the bottom of the DBC as shown in Fig. 2(b) for the geometrically boundary condition of the FEM. As a thermal boundary condition for the Si dies, a power cycling switching loss profile was applied as shown in Fig. 7(b). General material properties of numerical simulation are shown in Table 5. Material nonlinearity is calculated considering Tables 2 and 3, respectively. Fig. 7(c) illustrates the equivalent strain distributions of the power module; the strain clearly was distributed near the Cu clip

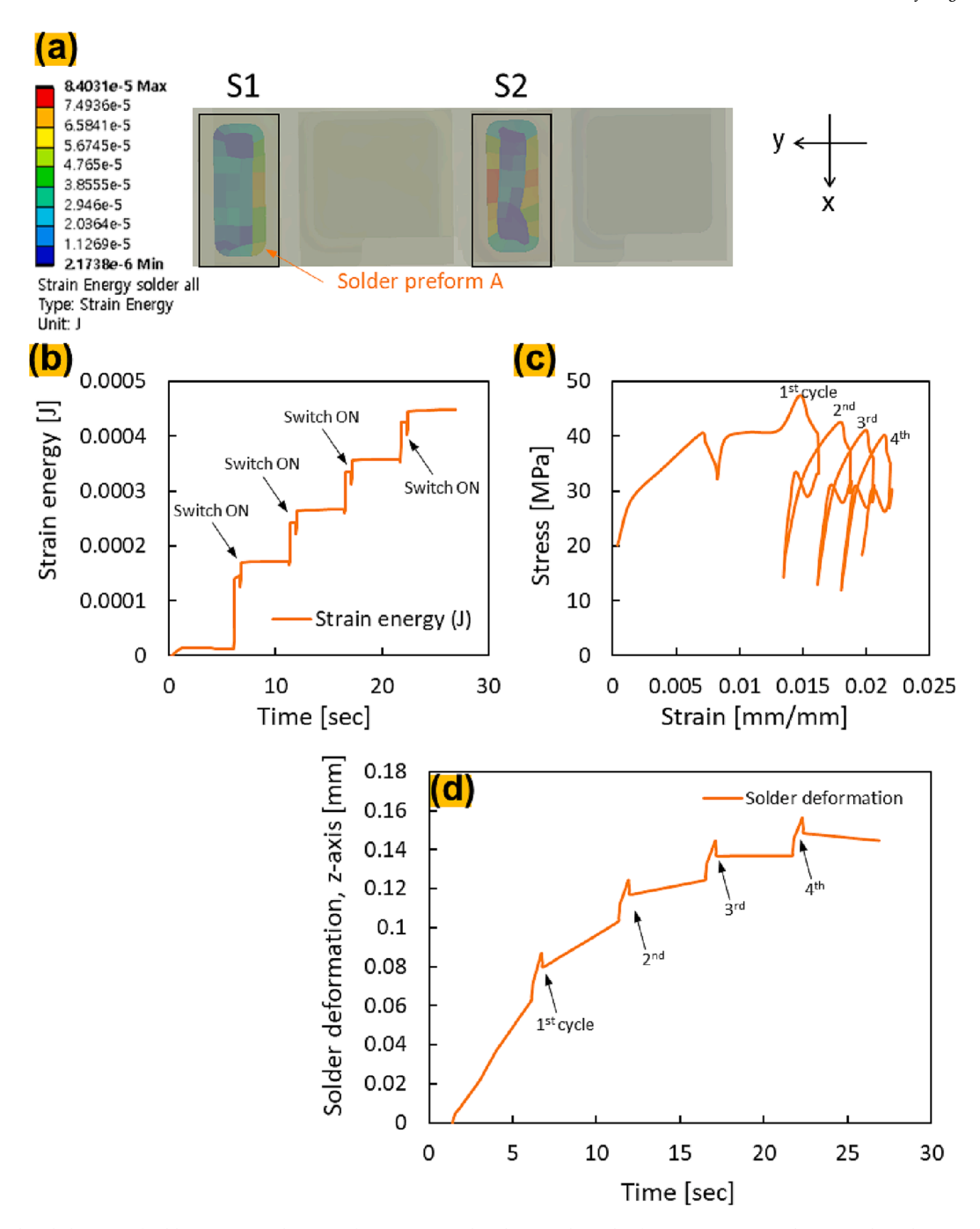


Fig. 9. Power cycling behaviors of solder joints. (a) the map of strain energy distribution, (b) a plot for strain energy evolution, and (c) the stress–strain hysteresis loop of solder joints, (d) deformation behavior of solder joints.

bonding. It was found that the EMC showed a significant strain distribution. The deformation behavior of the power module structure corresponding to the power cycling profile is shown in Fig. 7(d), and it can be confirmed that the deformation in the height (z-axis) direction gradually increases with repetitive power cycling. A warpage deformation at the top surface after 4 cycles of the EMC occurred, which was significantly deformed based on switching devices S1 and S2 as shown in Fig. 7(e). The light blue line is defined as amount of the warpage deformation in the ON state, and the orange line is defined as the amount of the warpage deformation when returning to the OFF state. The amount of peak deformation at the top surface of the EMC during ON switching and OFF states approached about $108~\mu m$, and the shape of the distribution was Gaussian distribution. The maximum difference between the amounts of warpage deformation of the bottom of the DBC

with the heat sink attached was about 30 μm when the power was turned ON and OFF. The reason why the deformation of the bottom of the DBC is not significant compared to the deformation of the top is that the bottom of the DBC is fixed to the heat sink. Therefore, the warpage of power modules clearly originated from the repetitive switching operations of the power semiconductors. In order to understand the mechanical behavior of the Cu clip due to such bending deformation, section A-A' was investigated. Fig. 7(f) displays the stress distribution of the plane A-A' cross-section, which can be confirmed that a stress of more than 200 MPa occurs in the Cu clip. The strain behavior of the EMC and Cu clips is shown in Fig. 8, and a large difference in the strain was observed when the two undergo power cycling. In here, strain can be calculated as:

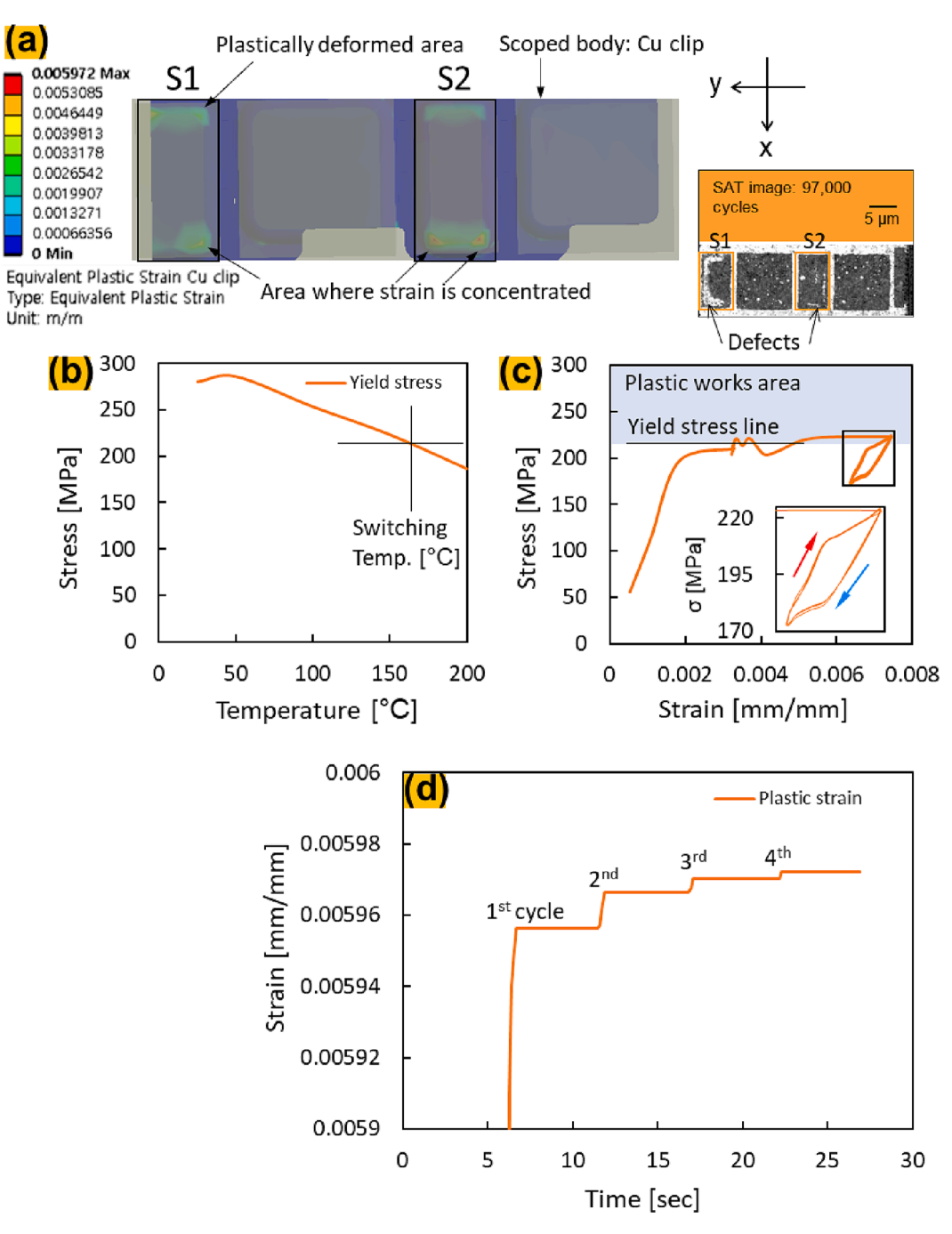


Fig. 10. Power cycling behaviors of the Cu clip. (a) the map of plastic strain distributions, (b) temperature dependence yield stress of the pure Cu [15], and (c) stress–strain hysteresis loop of the Cu clip, and (d) plastic behavior plot of the Cu clip.

$$\varepsilon = \delta l/l_0 \tag{28}$$

where l_0 denotes the initial length, and δl is the deformed length. In this study, total strain (ε_{total}) is constitutive as:

$$\varepsilon_{total} = \varepsilon_e + \varepsilon_p + \varepsilon_c \tag{29}$$

where ε_e is the term of the elastic strain, ε_p denotes the term of the plastic strain, and ε_c is the creep strain term. In addition, the EMC tended to gradually increase strain with each cycle of power cycling. In addition, it can be seen that the stress distributions of Cu clips were remarkable around the region where the strain distributions of EMC were remarkable. Thermal expansion mismatch between Cu clip and EMC, the stress gradient $d\sigma_f/dT$ can be described as follows [41]:

$$\frac{d\sigma_f}{dT} = \left[\frac{E_f}{(1 - v_f)}\right] * (\alpha_s - \alpha_f)$$
(30)

the stress gradient is the product between the biaxial modulus of the Cu clip, where E_f denotes elastic modulus, and v_f the Poisson's ratio of the Cu clip, and the expansion mismatch between the EMC: α_s and the Cu clip: α_f . In fact, the coefficient of thermal expansion (CTE) mismatch between Cu and EMC applied in this study is 113 ppm. Moreover, in the case of Si and AlN, in which the CTE mismatch with EMC was more severe, it can be confirmed that the stress of higher intensity was distributed.

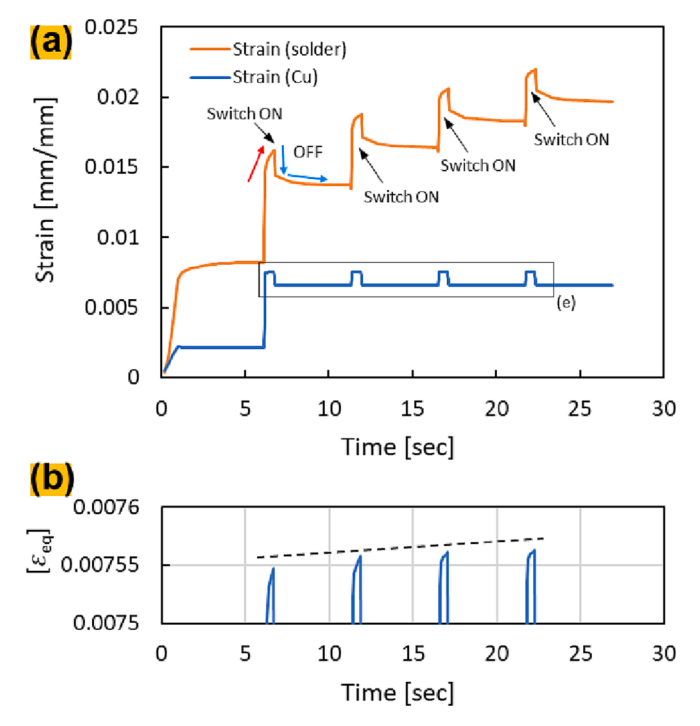


Fig. 11. (a) Comparison of strain behaviors depending on power cycles of the Cu clip and solder joint, (b) strain behavior plot of the Cu clip.

4.2. A contribution of solder joint behaviors

The solder creep behavior or mechanical degradation has been a significant issue in determining the lifespan of electronic products for the past decades [42–45]. Therefore, this section focuses on the contribution of solder joints to the deformation behavior at the scale of power modules. Fig. 9(a) represents the mechanical behavior of solder joint reliability, which displays a strain energy map; the intensity at the corner of the solder was remarkable. The strain energy is defined that when a force is applied to a material, the energy stored inside the material. Part of the total work caused by force acting on the object was used for plastic deformation, which permanently deforms the object, and the rest is accumulated as strain energy [15]. The formula of strain energy can be represented as follows:

$$U = \frac{1}{2} V \sigma \varepsilon \tag{31}$$

where σ is stress, ε is strain, and V is the volume of material, respectively. The stress is defined as $\sigma = E^*\varepsilon$ by Hooke's law relational expression, which can be derived by [15]:

$$U = \frac{V}{2E}\sigma^2 \tag{32}$$

in here, *E* is Young's modulus.

The strain energy accumulated in the solder joint was gradually increased depending on the power cycling number as shown in Fig. 9(b). The first power cycle caused 0.00017057 J (=0.17057 mJ) of the strain energy in solder joints, which strain energy was maintained until the

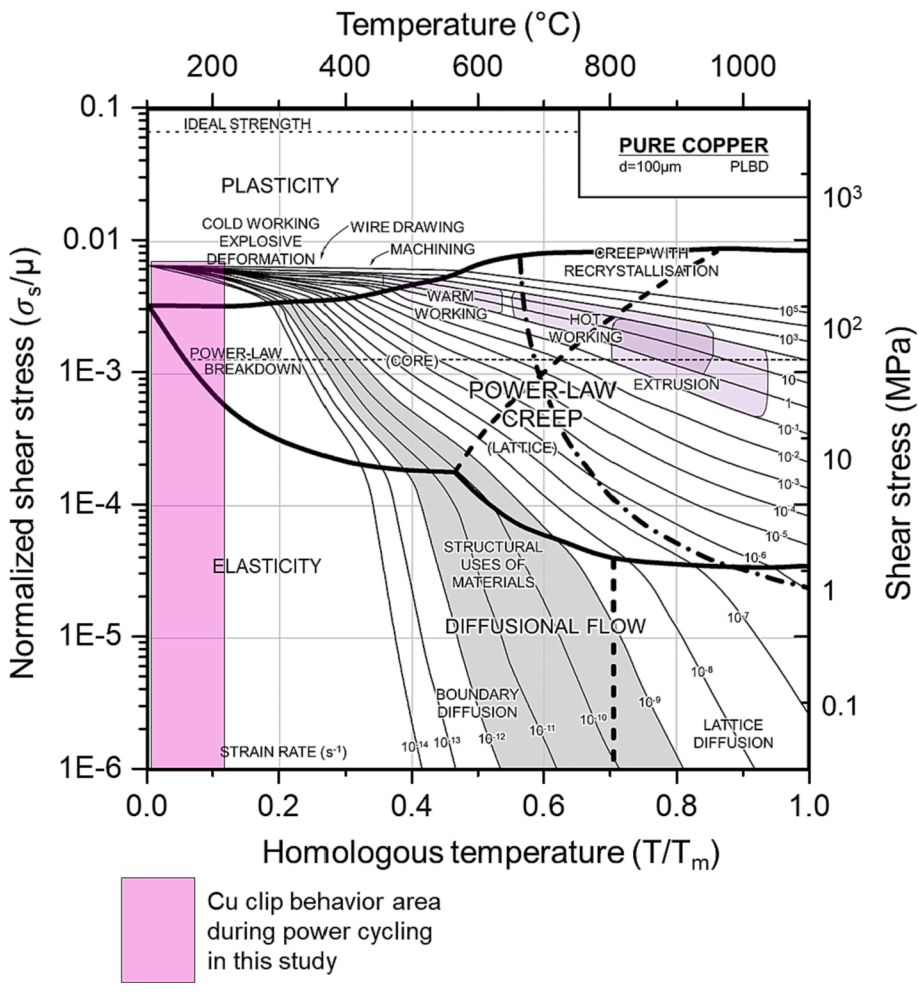


Fig. 12. Deformation mechanism map (DMM) of the pure Cu.

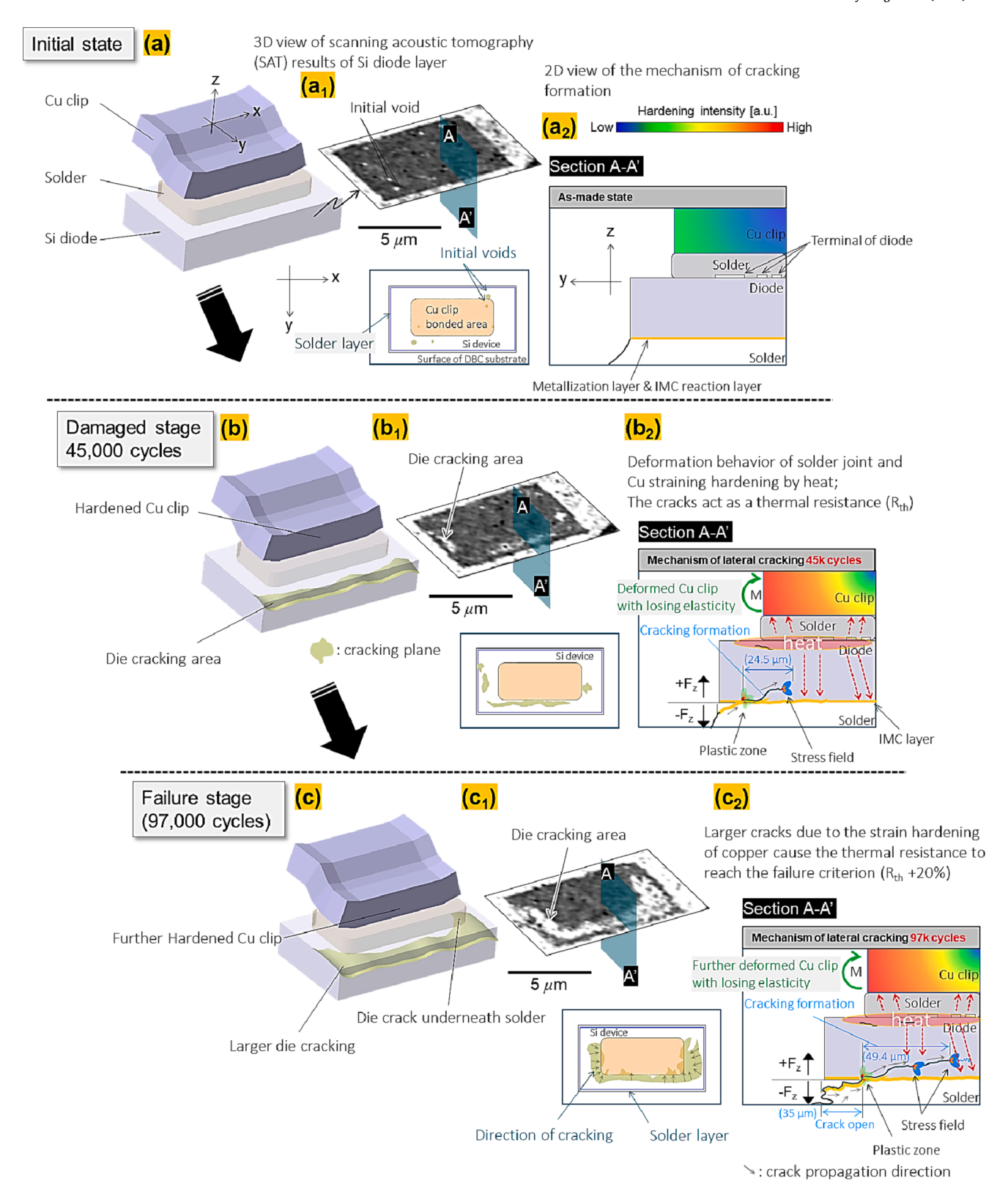


Fig. 13. Failure mechanism of the power module; the strain hardening of the Cu clip directly affects the failure of the power module. (a) Schematic 3D model of the initial state of the Cu clip interconnected solder and Si diode, (a_1) its SAT inspection result of the Si diode layer, and (a_2) 2D view of the section A-A' on (a_1) ; (b) schematic description of the damaged stage (45 k cycles) of the Cu clip interconnected solder and Si diode, (b_1) its SAT inspection result of the Si diode layer, and (b_2) 2D view of the mechanism of cracking in the section A-A' on (b_1) ; (c) schematic description of failure stage (97 k cycles) of the Cu clip interconnected solder and Si diode, (c_1) their SAT inspection result of the Si diode layer, and (c_2) 2D section view of the mechanism of cracking in the section A-A' on (c_1) .

next switch ON, and then strain energy increased by 42.9% of 0.00024377 J (i.e., 0.24377 mJ) was induced by the second cycle. With this trend, the strain energy of the solder was increased stepwise. Fig. 9 (c) depicts the stress-strain hysteresis loop of solder joints, each loop in the curve corresponds to 1 cycle. The hysteresis loop is considered to be stable as the cycles increase. However, it can be seen that the total strain of the solder joint gradually increases even if the cycle is repeated, which can be caused internal damage to the power module structural system. Fig. 9(d) shows the deformation behavior of solder joints depending on power cycles, and it tended to increase by about 20 µm for each repetitive power cycle. These solder contributions not only affect the solder joint reliability, but they can also have a significant impact on the material behavior of other elements in integrated power module structures. For this reason, the power module inside is constrained due to the characteristics of the transfer molded power module, and the bottom DBC substrate is attached to the heat sink, so the deformation behavior of the solder joints can affect the power semiconductor device and Cu clip mechanically.

4.3. The mechanism of Cu clip strain hardening

Strain hardening of the Cu clip by thermal fatigue showed a significant difference in the thermal resistance performance of the power module, which was experimentally found to be an important factor in determining the reliability of the power module. FEM simulation results revealed areas of plastic strain distributions after the power cycling process with damage concentrations at the outer sites of the Cu clip interface as displayed in Fig. 10(a). The plastic strain distribution of the Cu clip was obviously concentrated in the area corresponding to the diecracking region found in non-destructive inspection (SAT). This means that directly related to the cracking of the die and the plastic deformation behavior of the Cu clip. The stress-strain hysteresis loop and the yield stress at different temperatures were investigated to determine whether the plastic deformation of the Cu clip by power cycling was sufficient to cause grain refinements (see Fig. 10(b, c)). The yield stress at the power cycling temperature was found to exceed about 210 MPa, and the Cu clip of the transfer molded power module was shown to undergo an area of plastic works exceeding the yield strength due to power cycling. In Fig. 10(d), as the power cycling increased, the plastic strain of the Cu clip gradually increased. This means that dislocations can accumulate on the Cu clip as power cycling tests. To further discussed the strain behaviors of the Cu clip attributed to the creep effects of the solder joint, the total strain behavior of the Cu clip and solder joint was plotted in Fig. 11(a). The strain of the solder joint showed a tendency to gradually increase as the strain energy increased, and even was a significantly higher value than that of the Cu clip. Fig. 11(b) stands for the strain behaviors of the Cu clip, which is a magnified area in Fig. 11 (a). Surprisingly, a tendency to gradually increase by 0.13% per 4 cycles from 0.00755 in 1 cycle to 0.00756 in 4 cycles was observed. Therefore, the results of the numerical simulation verified that the Cu clip exhibited plastic behavior during power cycling, which sufficiently supports the reason for the experimentally revealed cause of grain refinements.

The deformation mechanism map (DMM) was investigated to further understand whether the Cu clip physically undergoes plastic deformation or recrystallization under the operating conditions of the power module. Fig. 12 illustrates the deformation mechanism map of pure Cu. Deformation mechanism maps (DMM) have been established since Ashby's work [46] in 1972 to delineate the dominant deformation mechanism under different combinations of temperature, stress, and grain size, which are then used to guide the optimization of processing parameters for use in bulk materials. The magenta color box corresponds to the region experienced by the Cu clip during the power cycling test in this study. Obviously, in the ON state of the power module of the current structure, it can be understood that the Cu clip experiences the area of cold working, explosive deformation and power law creep. Therefore, it is clear from the discussion of microstructures in the previous section

that the evolution of Cube texture components and grain refinements, both of which can occur in the typical cold working of Cu alloys, are caused by the thermo-mechanical response that occurs during power module operations.

4.4. Failure mechanism of the power module: die cracking

This section is discussed to clarify the mechanism by which the strain hardening of the Cu clip directly affects the failure of the power module. In DBC substrates, repeated thermal cycles have been studied extensively as a fatal cause of transverse cracks in the ceramic layer [12,47–50]. In particular, recent studies have well explained the mechanism by which the Cu layer forming DBC undergoes strain hardening by repeated thermal cycles. In the previous study, Patrick Gaiser et al. [10] mentioned that a prerequisite for predicting the crack propagation path is the correct modeling of the evolution of the stress and strain fields over thermal cycles. This obviously is a significant factor in the study of cracks and should be treated carefully. However, in this study, rather than predicting the crack path of ceramics, when a power module undergoes thermomechanical fatigue (TMF) by power cycling, what behaviors do the components of the module, including the Cu clip, cause, and how this behavior leads to failure.

From the results of the previous section, the solder joints of the power module undergoing PCTs exhibited periodic deformation behavior in the thickness direction (i.e., warpage), and this deformation tended to increase gradually. This bending behavior can also affect the Cu clip, and due to this, the structure of the Cu clip, which is gradually hardened, can be further deformed without returning to its original position. For this reason, die cracking can be induced if the deformation of the Si die limit is exceeded, which is remarkably low in ductility compared to solder joints or Cu clips. This die cracking often occurs in electronic devices and is a major factor in increasing thermal resistance [1,51]. Fig. 13 summarizes the strain hardening behavior and die cracking mechanism of these Cu clips. Fig. 13(a-a2) illustrates the initial state of the power module structure, which has just an initial minor void as a defect. Fig. 13(b) depicts the 3D model of the damaged stage (i.e., 45,000 cycles) of the Cu clip interconnected solder and Si diode. Here, the mustard-colored plane through the Si diode has defined a crack. As a result of SAT analysis, this crack region was clearly created in the Si die, and was formed around the periphery where the Cu clip was attached as displayed in Fig. 13(b₁). These cracks are suggested to be caused by the phenomenon that the Cu clip tries to deform by repetitive heat further while strain hardening and not returning to its original position as shown in Fig. 13(b₂). In other words, the more it tries to become convex in the thickness direction in the deformed state, the more cracks may occur in the Si die that can no longer withstand the strain (i.e., $+F_z$ > limitation of the Si die). Fig. 13(c) describes the 3D view model during the failure stage, which has further expanded the cracking plane and even developed up to the solder layer. In the SAT analysis result (see Fig. $13(c_1)$), the extended crack surface can be confirmed more clearly. Fig. 13(c₂) represents the 2D section view of the mechanism of cracking in sections A-A' on (c1). Due to larger cracks (i.e. cracks are air: 0.025 W/mK of the thermal conductivity), the thermal resistance can be further increased, which is the main cause of failure. Considering the linear increase in thermal resistance, the strain hardening of the Cu clip may have already reached a saturation state before 45,000 cycles. Also, if heat is applied to the Cu clip while the strain hardening is already saturated, the Cu will try to expand further and load the brittle Si die, causing gradual die cracking failure.

5. Conclusions

Operations of the power module have been experimentally verified that even bare Cu clip wire interconnections, not DBC, can cause unexpected strain hardening due to thermomechanical fatigue behavior. The molded EMC with the solder joint dramatically changed the crystallographic microstructure of Cu clips by geometrically constraining the internal structure during power cycling operation, which is direct evidence causing strain hardening of the Cu clip bonding. From the FEM simulation results, we have numerically understood that the Cu clip originates plastic deformation during power cycling tests. In addition, in this process, the viscoplastic behavior of the solder joint increased the strain energy in a stepwise manner, which directly affects the warpage of the power module structure including the Cu clip. Namely, strain hardening can occur significantly in bare Cu clips due to geometrical constraints, even if there is no strong bonding like DBC substrates.

Declaration of Competing Interest

The authors declare that they have no known competing financial interests or personal relationships that could have appeared to influence the work reported in this paper.

Data availability

No data was used for the research described in the article.

Acknowledgments

This study has been conducted with the support of the Korea Institute of Industrial Technology as "Development of root technology for multiproduct flexible production (KITECH EO-23-0008). The authors are grateful to HYUNDAI MOBIS Co., Ltd.

References

- [1] Kim D, Lee B, Lee T-I, Noh S, Choe C, Park S, et al. Power cycling tests under driving ΔTj = 125 ∘C on the Cu clip bonded EV power module. Microelectron Reliab 2022;138:114652. https://doi.org/10.1016/j.microrel.2022.114652.
- [2] Pavlicek N, Vater S, Liu C, Loisy JY, Salvatore G, Mohn F, et al. Power module platform for automotive reliability requirements. In: 2019 21st Eur. Conf. Power Electron. Appl. EPE 2019 ECCE Eur.; 2019. p. 1–10. doi: 10.23919/ EPE.2019.8915223.
- [3] Kim D, Won MS, Jang J, Kim S, Oh C. Development of solderable layer on power MOSFET for double-side bonding. Microelectron Reliab 2022;129:114482. https://doi.org/10.1016/j.microrel.2022.114482.
- [4] Ivanova M, Avenas Y, Schaeffer C, Dezord JB, Schulz-Harder J. Heat pipe integrated in direct bonded copper (DBC) technology for cooling of power electronics packaging. IEEE Trans Power Electron 2006;21:1541–7. https://doi. org/10.1109/TPEL.2006.882974.
- [5] Durand C, Klingler M, Bigerelle M, Coutellier D. Solder fatigue failures in a new designed power module under Power Cycling. Microelectron Reliab 2016;66: 122–33. https://doi.org/10.1016/j.microrel.2016.10.002.
- [6] Tokuyama T, Mima A, Takagi Y, Matsushita A. Low-inductance double-sided cooling power module with branched lead frame terminals for EV traction inverter. In: ECCE 2020 - IEEE Energy Convers. Congr. Expo.; 2020, p. 3987–91. doi: 10.1109/ECCE44975.2020.9235880.
- [7] Sugiura K, Iwashige T, Tsuruta K, Chen C, Nagao S. Reliability evaluation of SiC power module with sintered Ag Die - attach and stress - relaxation structure. In: IEEE Trans Components, Packag Manuf Technol 2019. p. 1. doi: 10.1109/ TCPMT.2019.2901543.
- [8] Park S, Nagao S, Sugahara T, Suganuma K. Heel crack propagation mechanism of cold-rolled Cu/Al clad ribbon bonding in harsh environment. J Mater Sci Mater Electron 2015;26:7277–89. https://doi.org/10.1007/s10854-015-3355-y.
- [9] Kim D, Yamamoto Y, Nagao S, Wakasugi N. Measurement of heat dissipation and thermal-stability of power modules on DBC substrates with various ceramics by SiC micro-heater chip system and ag sinter joining. Micromachines n.d.:1–11.
- [10] Gaiser P, Klingler M, Wilde J. The influence of strain hardening of copper on the crack path in Cu/Al2O3/Cu direct bonded copper substrates. Int J Fatigue 2020; 140:105821. https://doi.org/10.1016/j.ijfatigue.2020.105821.
- [11] Xu L, Liu S, Wang M, Zhou S. Crack initiation and propagation mechanism of Al2O3-DBC substrate during thermal cycling test. Eng Fail Anal 2020;116:104720. https://doi.org/10.1016/j.engfailanal.2020.104720.
- [12] Pietranico S, Pommier S, Lefebvre S, Pattofatto S. Thermal fatigue and failure of electronic power device substrates. Int J Fatigue 2009;31:1911–20. https://doi. org/10.1016/j.ijfatigue.2009.03.011.
- [13] Utschig T, Descher P, Rauer M, Schwöbel A, Schnee D. Metal ceramic substrates for highly reliable power modules - not only in electric vehicles. InterCeram Int Ceram Rev 2020;69:20–5. https://doi.org/10.1007/s42411-020-0086-8.
- [14] Durand C, Klingler M, Coutellier D, Naceur H. Power cycling reliability of power module: a survey. IEEE Trans Device Mater Reliab 2016;16:80–97. https://doi.org/ 10.1109/TDMR.2016.2516044.

- [15] Kim D, Choe C, Chen C, Lee S, Lee SJ, Park S, et al. The Σ3 twin dependence of thermo-mechanical fatigue of a polycrystalline high-purity Cu film. Int J Fatigue 2021;150:106331. https://doi.org/10.1016/j.ijfatigue.2021.106331.
- [16] Choi UM, Jørgensen S, Iannuzzo F, Blaabjerg F. Power cycling test of transfer molded IGBT modules by advanced power cycler under different junction temperature swings. Microelectron Reliab 2018;88–90:788–94. https://doi.org/ 10.1016/j.microrel.2018.07.002.
- [17] Choi UM, Jorgensen S, Blaabjerg F. Advanced accelerated power cycling test for reliability investigation of power device modules. IEEE Trans Power Electron 2016; 31:8371–86. https://doi.org/10.1109/TPEL.2016.2521899.
- [18] Yasui K, Hayakawa S, Nakamura M. Improvement of power cycling reliability of 3. 3kV full-SiC power modules with sintered copper technology for T j, max = 175 ° C. In: 2018 IEEE 30th Int. Symp. Power Semicond. Devices ICs, IEEE; 2018. p. 455-8.
- [19] Durand C, Klingler M, Coutellier D, Naceur H. Confrontation of failure mechanisms observed during Active Power Cycling tests with finite element analyze performed on a MOSFET power module. In: 2013 14th Int Conf Therm Mech Multi-Physics Simul Exp Microelectron Microsystems, EuroSimE 2013; 2013. doi: 10.1109/ EuroSimE.2013.6529900.
- [20] Durand C, Klingler M, Coutellier D, Naceur H. Failure mechanisms in chipmetallization in power applications. In: 2014 15th Int. Conf. Therm. Mech. Multi-Physics Simul. Exp. Microelectron. Microsystems, EuroSimE 2014; 2014. p. 1–5. doi: 10.1109/EuroSimE.2014.6813772.
- [21] Zhang Z, Chen C, Suetake A, Ishino H, Sampei H, Endo T, et al. Online condition monitoring of solder fatigue in a clip-bonding SiC MOSFET power assembly via acoustic emission technique. IEEE Trans Power Electron 2022:1–10. https://doi. org/10.1109/tpel.2022.3209740.
- [22] Kim D, Nagao S, Chen C, Wakasugi N, Yamamoto Y, Suetake A, et al. Online thermal resistance and reliability characteristic monitoring of power modules with Ag sinter joining and Pb, Pb-free solders during power cycling test by SiC TEG chip. IEEE Trans Power Electron 2021;36:4977–90. https://doi.org/10.1109/ TPEL.2020.3031670.
- [23] Zhang Z, Chen C, Suetake A, Hsieh MC, Iwaki A, Suganuma K. Pressureless and low-temperature sinter-joining on bare Si, SiC and GaN by a Ag flake paste. Scr Mater 2021;198:113833. https://doi.org/10.1016/j.scriptamat.2021.113833.
- [24] Girard G, Martiny M, Mercier S. Experimental characterization of rolled annealed copper film used in flexible printed circuit boards: Identification of the elasticplastic and low-cycle fatigue behaviors. Microelectron Reliab 2020;115:1–10. https://doi.org/10.1016/j.microrel.2020.113976.
- [25] Xu L, Wang M, Zhou Y, Qian Z, Liu S. An optimal structural design to improve the reliability of Al2O3-DBC substrates under thermal cycling. Microelectron Reliab 2016;56:101–8. https://doi.org/10.1016/j.microrel.2015.11.013.
- [26] Yan L, Yao J, Dai Y, Zhang S, Bai W, Gao K, et al. Study of thermal stress fluctuations at the die-attach solder interface using the finite element method. Electron 2022;11. doi: 10.3390/electronics11010062.
- [27] He X, Yao Y, Keer LM. A rate and temperature dependent unified creep-plasticity model for high strength steel and solder alloys. Mech Mater 2017;106:35–43. https://doi.org/10.1016/j.mechmat.2017.01.005.
- [28] Chen G, Hu T, Xie M, Yang J, Xu W. A new unified constitutive model for SAC305 solder under thermo-mechanical loading. Mech Mater 2019;138. doi: 10.1016/j. mechmat.2019.103170.
- [29] Voet V, Van Loock F, De Fruytier C, Simar A, Pardoen T. Machine learning aided modelling of thermomechanical fatigue of solder joints in electronic component assemblies. Int J Fatigue 2022:107298. doi: 10.1016/j.ijfatigue.2022.107298.
- [30] Zhang L, Han J guang, Guo Y huan, He C wen. Effect of rare earth Ce on the fatigue life of SnAgCu solder joints in WLCSP device using FEM and experiments. Mater Sci Eng A 2014;597:219–24. doi: 10.1016/j.msea.2013.12.098.
- [31] Anand L. Constitutive equations for the rate-dependent deformation of metals at elevated temperatures. J Eng Mater Technol Trans ASME 1982;104:12–7. https:// doi.org/10.1115/1.3225028.
- [32] Zhang ZN, Wang GZ, Chen L, Wilde J, Becker K. Viscoplastic Anand model for solder alloys and its application. Solder Surf Mt Technol 2000;12:31–6.
- [33] Motalab M, Cai Z, Suhling JC, Lall P. Determination of Anand constants for SAC solders using stress-strain or creep data. In: Intersoc. Conf. Therm. Thermomechanical Phenom. Electron. Syst. ITHERM, vol. C; 2012. p. 910–22. doi: 10.1109/TTHERM.2012.6231522.
- [34] Lutz J, Herrmann T, Feller M, Bayerer R, Licht T, Amro R. Power cycling induced failure mechanisms in the viewpoint of rough temperature environment. In: CIPS 2008 - 5th Int. Conf. Integr. Power Electron. Syst. Proc.; 2008. p. 55–8.
- [35] Jamaati R. Unexpected Cube texture in cold rolling of copper. Mater Lett 2017;202: 111–5. https://doi.org/10.1016/j.matlet.2017.05.054.
- [36] Hall EO. The deformation and ageing of mild steel: III discussion of results. Proc Phys Soc Sect B 1951;64:747–53.
- [37] The cleavage strength of polycrystals. J Iron Steel Inst 1953;174:25–8.
- [38] Kong J, Haché MJR, Tam J, McCrea JL, Howe J, Erb U. On the extrinsic hall-petch to inverse Hall-Petch transition in nanocrystalline Ni-Co electrodeposits. Scr Mater 2022;218. doi: 10.1016/j.scriptamat.2022.114799.
- [39] Tiryakioğlu M. On the relationship between Vickers hardness and yield stress in Al-Zn-Mg-Cu Alloys. Mater Sci Eng A 2015;633:17–9. https://doi.org/10.1016/j.msea.2015.02.073.
- [40] Pourhamid R, Shirazi A. Microstructural evolution and mechanical behaviors of equal channel angular pressed copper. Proc Inst Mech Eng Part C J Mech Eng Sci 2020;234:171–9. https://doi.org/10.1177/0954406219872520.
- [41] Bigl S, Wurster S, Cordill MJ, Kiener D. Advanced characterisation of thermomechanical fatigue mechanisms of different copper film systems for wafer

- metallizations. Thin Solid Films 2016;612:153-64. https://doi.org/10.1016/j.
- [42] Sakane M, Shiratsuchi T, Tsukada Y. Grain boundary sliding model for assessing creep-fatigue life of Sn37Pb eutectic solder. Int J Fatigue 2021;146:106132. https://doi.org/10.1016/j.ijfatigue.2020.106132.
- [43] Yang XJ, Chow CL, Lau KJ. Time-dependent cyclic deformation and failure of 63Sn/37Pb solder alloy. Int J Fatigue 2003;25:533–46. https://doi.org/10.1016/ S0142-1123(02)00150-0.
- [44] Zhao J, Miyashita Y, Mutoh Y. Fatigue crack growth behavior of 96.5Sn-3.5Ag lead-free solder. Int J Fatigue 2001;23:723–31. https://doi.org/10.1016/S0142-1123(01)00034-2.
- [45] Towashiraporn P, Gall K, Subbarayan G, McIlvanie B, Hunter BC, Love D, et al. Power cycling thermal fatigue of Sn-Pb solder joints on a chip scale package. Int J Fatigue 2004;26:497–510. https://doi.org/10.1016/j.ijfatigue.2003.09.004.
- [46] Ashby MF. A first report on deformation-mechanism maps. Acta Metall 1972;20: 887–97. https://doi.org/10.1016/0001-6160(72)90082-X.

- [47] Dupont L. Contribution à l'étude de la durée de vie des assemblages de puissance dans des environnements haute température et avec des cycles thermiques de grande amplitude. 2006.
- [48] Yoshino Y, Ohtsu H, Shibata T. Thermally induced failure of copper-bonded alumina substrates for electronic packaging. J Am Ceram Soc 1992;75:3353–7. https://doi.org/10.1111/j.1151-2916.1992.tb04433.x.
- [49] Yoshino Y, Ohtsu H. Interface structure and bond strength of copper-bonded alumina substrates. J Am Ceram Soc 1991;74:2184–8. https://doi.org/10.1111/ j.1151-2916.1991.tb08281.x.
- [50] Choe C, Chen C, Noh S. Thermal shock performance of DBA / AMB substrates plated by Ni and Ni – P layers for high-temperature applications of power device modules. Materials (Basel) 2018;11:2394. https://doi.org/10.3390/ma11122394.
- [51] Annaniah L, Devarajan M, San TK. An investigation on die crack detection using Temperature Sensitive Parameter for high speed LED mass production. Results Phys 2017;7:3882–91. https://doi.org/10.1016/j.rinp.2017.09.036.